Journal of Medicinal Chemistry

Article

pubs.acs.org/jmc

Development of [^{18}F]-Labeled Pyrazolo[4,3-*e*]-1,2,4-triazolo[1,5-*c*]pyrimidine (SCH442416) Analogs for the Imaging of Cerebral Adenosine A_{2A} Receptors with Positron Emission Tomography

Shivashankar Khanapur,[†] Soumen Paul,[†] Anup Shah,[‡] Suresh Vatakuti,[§] Michel J. B. Koole,[†] Rolf Zijlma,[†] Rudi A. J. O. Dierckx,[†] Gert Luurtsema,[†] Prabha Garg,[‡] Aren van Waarde,[†] and Philip H. Elsinga*[,†]

[†]Department of Nuclear Medicine and Molecular Imaging, University Medical Center Groningen, University of Groningen, Groningen, The Netherlands

[‡]Computer Centre, National Institute of Pharmaceutical Education and Research, SAS Nagar, Mohali, India

[§]Department of Pharmacokinetics, Toxicology and Targeting, University of Groningen, Groningen, The Netherlands

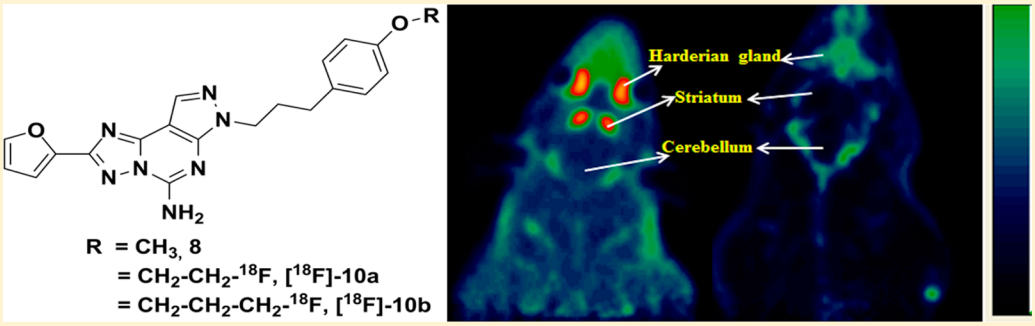

ABSTRACT: Cerebral adenosine A_{2A} receptors (A_{2A}Rs) are attractive therapeutic targets for the treatment of neurodegenerative and psychiatric disorders. We developed high affinity and selective compound **8** (SCH442416) analogs as in vivo probes for A_{2A}Rs using PET. We observed the A_{2A}R-mediated accumulation of [^{18}F]fluoropropyl ([^{18}**F**]-**10b**) and [^{18}F]fluoroethyl ([^{18}**F**]-**10a**) derivatives of **8** in the brain. The striatum was clearly visualized in PET and in vitro autoradiography images of control animals and was no longer visible after pretreatment with the A_{2A}R subtype-selective antagonist KW6002. In vitro and in vivo metabolite analyses indicated the presence of hydrophilic (radio)metabolite(s), which are not expected to cross the blood-brain-barrier. [^{18}**F**]-**10b** and [^{18}**F**]-**10a** showed comparable striatum-to- cerebellum ratios (4.6 at 25 and 37 min post injection, respectively) and reversible binding in rat brains. We concluded that these compounds performed equally well, but their kinetics were slightly different. These molecules are potential tools for mapping cerebral A_{2A}Rs with PET.

INTRODUCTION

Adenosine, an endogenous signaling substance, is a purine ribonucleoside that is composed of adenine (purine base) and ribose (sugar molecule).[1] It functions as a cytoprotectant and neuromodulator in response to organ and tissue stresses under both physiological and pathological conditions.[2] In the brain, adenosine plays an important role in the regulation of both neuronal and glial cell functions. Furthermore, it counteracts glutamate excitotoxicity and cytokine-induced apoptosis.[3] Its actions are mediated through the activation of four subtypes of G-protein coupled adenosine receptors (ARs), namely A_1, A_{2A}, A_{2B}, and A_3.[2]

Adenosine A_1 receptors (A_1Rs) and adenosine A_3 receptors (A_3Rs) are G-protein-coupled binding sites for adenosine that inhibit adenylyl cyclase, whereas adenosine A_{2A} receptors (A_{2A}Rs) and adenosine A_{2B} receptors (A_{2B}Rs) stimulate adenylyl cyclase via G_S proteins and promote the formation of the second messenger cyclic adenosine monophosphate (cAMP).[4] The subtypes differ in size (A_1, A_{2A}, A_{2B}, and A_3 consist of 326, 409, 328, and 318 amino acids, respectively) and exhibit unique tissue distributions.[5]

Over the last 30 years, the most extensively studied AR subtypes are the biochemically and pharmacologically well-characterized high-affinity A_1Rs and A_{2A}Rs. Adenosine activates these receptors at nanomolar concentrations.[2] A_1Rs are widely distributed in the human brain, with the highest densities being found in the hippocampus, cerebral cortex, thalamic nuclei, and dorsal horn of spinal cord, whereas A_{2A}Rs are highly expressed in the dopamine-rich regions of the brain, and the highest levels of A_{2A}R expression occur in the striatum (caudate-putamen, nucleus accumbens, and olfactory tubercle), globus pallidus and substantia nigra.[6−9] Lower levels of A_{2A}Rs occur in the

Received: May 23, 2014
Published: July 25, 2014

dx.doi.org/10.1021/jm500700y | *J. Med. Chem.* 2014, 57, 6765−6780

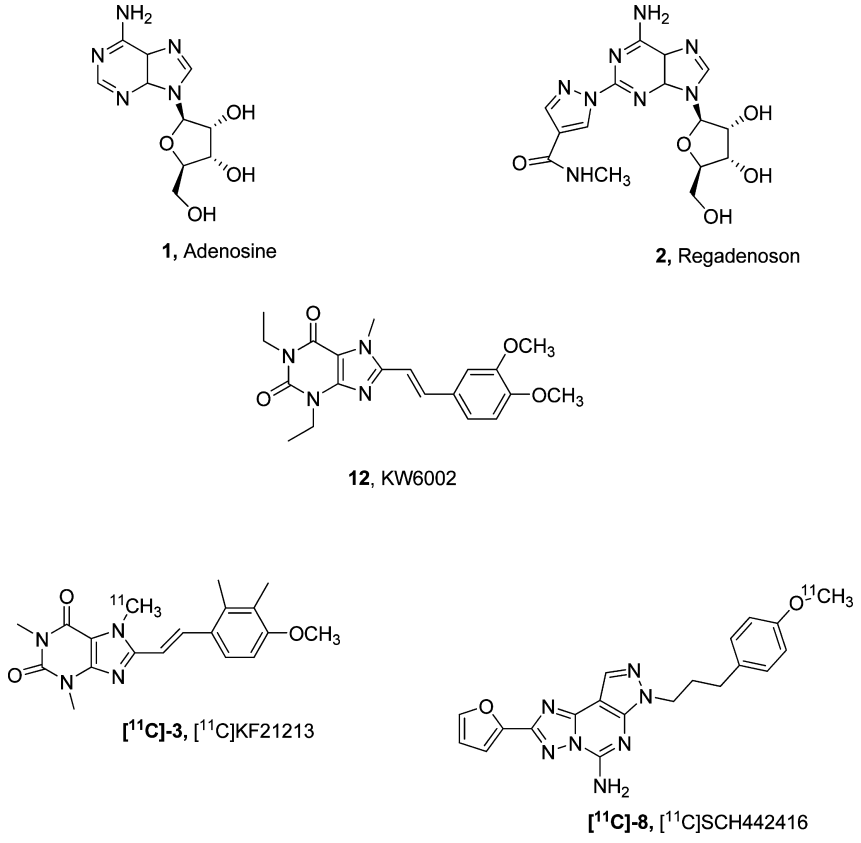

Figure 1. Structures of some selected AR agonists, an antagonist KW6002, and $A_{2A}R$ PET imaging agents.

hippocampus, cerebral cortex, amygdala, cerebellum, brainstem, and hypothalamus.[10−13]

The activation of A_1Rs (e.g., by A_1R agonists) increases sleep, inhibits seizures, reduces anxiety, and promotes neuroprotection. On the other hand, A_1R antagonists are anxiolytics, are beneficial in the treatment of cognitive disorders, cardiac arrhythmia, asthma, and other respiratory disorders, and are therapeutic drugs for kidney protection.[14] $A_{2A}R$ agonists are implicated in tissue repair, which involves a series of coordinated and overlapping phases such as inflammation, wound healing, angiogenesis, and tissue reorganization.[15−17] The vasodilating effect of $A_{2A}R$ agonists (adenosine and regadenoson) has been fully validated (see Figure 1). Adenosine (Figure 1, compound **1**) is used for the treatment of paroxysmal supraventricular tachycardia,[3] whereas regadenoson (Figure 1, compound **2**) is currently marketed for use as a pharmacologic stress agent in (radionuclide) myocardial perfusion imaging.[18]

$A_{2A}Rs$ mediate potential neuroprotective and neurotoxic effects in addition to modulating dopaminergic neurotransmission in the basal ganglia through the antagonistic interactions between $A_{2A}Rs$ and dopamine D_2 receptors (D_2Rs).[19−21] However, their role in neurodegenerative diseases such as Parkinson's disease (PD) and Alzheimer's disease (AD) is highly controversial.[21] Nevertheless, based on preclinical studies, $A_{2A}R$ antagonists have potential benefits in the treatment of neurodegenerative and psychiatric disorders such as PD, AD, neuroinflammation, ischemia, spinal cord injury, drug addiction, and other conditions.[18,20−23] Moreover, recent epidemiological studies have established that the regular consumption of caffeine (a xanthine derivative and AR antagonist) is associated with a lower risk for developing PD[24] or AD.[25] Along with D_2Rs, $A_{2A}R$ antagonists attenuate the overactivity of the indirect dopamine pathway observed during PD, restore balance between the direct and indirect output pathways, and suppress the neurodegenerative process by modulating the activity of cortico-striato-pallido-thalamocortical (CSPTC) pathways.[20,26,27]

Positron emission tomography (PET) can noninvasively assess the functional status of CSPTC pathways in PD and related disorders.[28] High-affinity antagonistic radioligands that are selective for the $A_{2A}Rs$ can be used to assess changes in $A_{2A}R$ density during disease progression and to monitor the effects of therapy on these changes.[2] Moreover, they can be employed to assess the occupancy of the receptor population by therapeutic drugs in the human brain, which will allow the correlation of receptor occupancy with dose, drug/tracer plasma levels, and therapeutic effects.[2,18,29,30] We focused on $A_{2A}R$ antagonist core structures as PET ligands (instead of $A_{2A}R$ agonist structures) because agonist PET tracers may only bind to the high-affinity state of the receptors, resulting in a poor signal-to-noise ratio.[31] Moreover, the in vivo vulnerability to competition by endogenous adenosine may hamper the quantification of the total number of binding sites.[31]

The design and development of novel $A_{2A}R$ antagonist PET ligands is a key research topic because current xanthine-based tracers suffer from several disadvantages, including high nonspecific binding, low signal-to-noise ratios, and therefore, target sites in the brain are barely visible. Furthermore, the use of xanthine-based tracers suffer from a photoisomerization problem, low selectivity toward $A_{2A}R$.[2,29,32−38] On the basis of these considerations, nonxanthine compounds were developed and evaluated in many preclinical and clinical studies for the assessment of cerebral $A_{2A}Rs$.[18]

dx.doi.org/10.1021/jm500700y | J. Med. Chem. 2014, 57, 6765−6780

A high degree of selectivity and appropriate combinations of lipophilicity, molecular weight, and affinity are important in the development of ideal in vivo $A_{2A}R$ PET brain tracers.[39] For a compound to cross the blood-brain-barrier (BBB), a relatively small molecular weight (400 to 500 Da) and moderate lipophilicity (approximate range of log *P* is 2 to 3.5) are optimal.[39−41] High lipophilicity causes unacceptable binding to plasma proteins and lipid bilayers, resulting in high levels of nonspecific binding in the brain.[39] Low lipophilicity decreases the penetration of PET agents across the BBB. In addition, the tracer's affinity must balance the opposing goals of tight binding and significant washout from the brain. Furthermore, the easy and rapid (within 3 half-lives) incorporation of radionuclides into the appropriate precursor molecules is necessary. Finally, the formation of lipophilic radioactive metabolites should be negligible because the presence of resulting radiometabolites in the target tissue would impede the quantification of the PET data using kinetic models.[39,42]

Rodent studies with nonxanthine tracer 7-(3-(4-[^{11}C]-methoxyphenyl)propyl)-2-(2-furyl)pyrazolo[4,3-*e*]-1,2,4-triazolo[1,5-*c*]pyrimidine-5-amine [^{11}**C**]-**8** ([^{11}C]SCH442416; Figure 1)[43,44] and its 2-[^{18}F]fluoroethyl derivative [^{18}**F**]-**10a** ([^{18}F]MRS5425 = [^{18}F]FESCH in Scheme 3)[47,48] suggest their potential value for in vivo mapping of A_{2A}Rs.[43−48] However, high nonspecific binding and a lower striatum (target)-to-cerebellum (nontarget) ratios (4.6 for [^{11}**C**]-**8** at 15 min; no target-to-nontarget data available for [^{18}**F**]-**10a**) than [7-methyl-^{11}C](*E*)-8-(2,3-dimethyl-4-methoxystyryl)-1,3,7-trimethylxanthine [^{11}**C**]-**3** ([^{11}C]KF21213; a xanthine-based tracer, 10.5 at 60 min, Figure 1)[38] were associated with these tracers, and these compounds will require further evaluation in human subjects.[44,48] Furthermore, [^{11}**C**]-**3** (a tight binding tracer suffers from several limitations such as photoisomerization, an impaired kinetic profile, low BBB penetration, and poor water solubility.[2,44]

All of the A_{2A}R antagonist PET ligands that have been successfully evaluated in humans to date are [^{11}C]-labeled. The radioisotope ^{18}F has advantages of higher specific activity and a longer physical half-life (109.8 min vs 20.4 min) than [^{11}C] ligands; these advantages allow the tracer to be distributed to remote imaging centers without cyclotron facilities and to achieve longer biodistribution and scanning times for a better assessment of the dissociation rate constant (K_{off}).[48,49] On the basis of the above considerations, favorable docking results and because compound **8** demonstrated an appropriate lipophilicity for CNS imaging in addition to the highest A_{2A}R affinity and subtype-selectivity, the present study utilized **8** as a lead compound to develop a novel radiofluorinated A_{2A}R ligand. We designed and prepared an 7-(3-(4-(3-[^{18}F]-uoropropoxy)-phenyl)propyl)-2-(furan-2-yl)-7H-pyrazolo[4,3-*e*][1,2,4]-triazolo[1,5-*c*]pyrimidin-5-amine derivative [^{18}**F**]-**10b** ([^{18}F]FPSCH in Scheme 3) and compared its pharmacokinetics and biodistribution in healthy rats with those of [^{18}**F**]-**10a** and [^{11}**C**]-**8** to optimize the length of the fluoroalkyl chain, which could affect both A_{2A}R affinity and selectivity.

RESULTS

Molecular Docking. Table 1 shows the GOLD fitness scores and important interactions for the docked ligands. A molecular docking study was performed to elucidate the intermolecular interactions between the 7-(3-(4-methoxyphenyl)propyl)-2-(2-furyl)pyrazolo[4,3-*e*]-1,2,4-triazolo[1,5-*c*]pyrimidine-5-amine **8** (SCH442416, Scheme 2)

Table 1. Docking Analysis of A_{2A} Antagonists Using GOLD Software

S.No.	Compound Name	GOLD fitness Score	H-Bond (s)	π-π stacking
	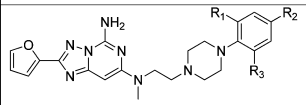			
1	Where R_1, R_2 = F and R_3 = H, Piperazine derivative of Triazolopyrimidine-I (**13**)	69.17	Asn253 (Furan O and NH_2)	Phe168
2	Where R_1, R_2, R_3 = F, Piperazine derivative of Triazolopyrimidine-II (**14**)	59.66		Phe168 and His250
3	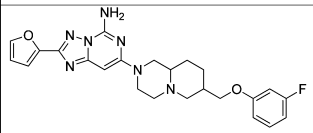 Bicyclic piperazine triazolotriazine derivative (**15**)	65.14	Asn253 (Furan O and NH_2), Leu267-NH_2	Phe168 and His250
4	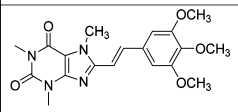 KF18446 (**16**)	51.35	Asn253(C=O), Thr68, Ile66	Phe168
5	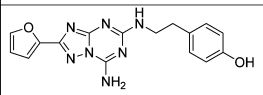 ZM241385 (**17**)	65.69	Asn253 (Furan O), Glu167 (OH)	His250
6	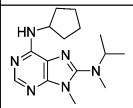 LUF5608 (**18**)	40.97	NA	Phe168
	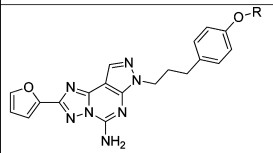			
7	Where R = CH_3, **8**	71.23	Asn253 (Furan O and NH_2)	Phe168 and His250
8	R = CH_2-CH_2-F, **10a**	69.86		
9	R = CH_2-CH_2-CH_2-F, **10b**	70.6		
10	Where R = CH_2-F, 7-(3-(4-(1-Fluoromethoxy)phenyl)propyl)-2-(furan-2-yl)-7H-pyrazolo[4,3-e][1,2,4]triazolo[1,5-c]pyrimidin-5-amine	69.46	Asn181 (Furan O), Asn253(NH_2)	Phe168, His250 and Trp246

derivatives and A_{2A}Rs. The major ligand binding interactions are both polar and hydrophobic in nature and occur with residues in trans-membrane domains 3, 5, 6, and 7. Residues from the second extracellular loop (ECL2) outline the upper part of the binding cavity (Figure 2B). In our study, 7-(3-(4-(2-fluoroethoxy)phenyl)propyl)-2-(furan-2-yl)-7H-pyrazolo[4,3-*e*][1,2,4]triazolo [1,5-*c*]pyrimidin-5-amine **10a** (FESCH, Scheme 2) and 7-(3-(4-(3-fluoropropoxy)phenyl)propyl)-2-(furan-2-yl)-7H-pyrazolo[4,3-*e*][1,2,4]triazolo[1,5-*c*]pyrimidin-5-amine **10b** (FPSCH, Scheme 2) had binding modes that were similar to the cocrystallized 4-(2-[7-amino-2-(2-furyl)[1,2,4]-triazolo[2,3-*a*][1,3,5]triazin-5-yl-amino]ethyl)phenol **17** (ZM241385, fifth compound in Table 1) conformation (Figure 2A), including the important hydrogen bond interactions with

dx.doi.org/10.1021/jm500700y | J. Med. Chem. 2014, 57, 6765−6780

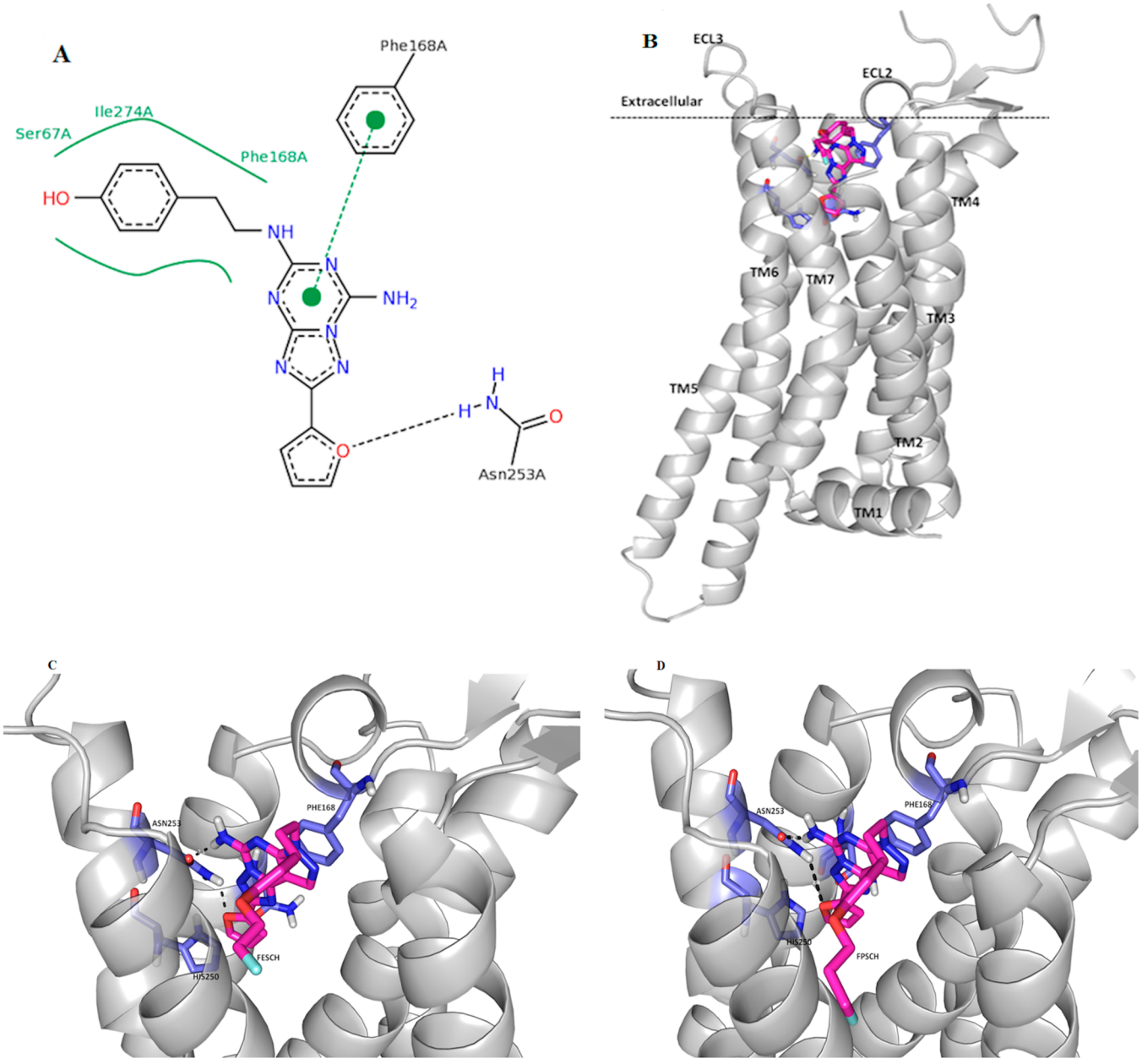

Figure 2. (A) Interaction between antagonist **17** and $A_{2A}R$ binding site residues. (B) Docked conformation of **10b** with $A_{2A}R$, viewed from the membrane and extracellular (ECL) sides, showing ECL2-folded into the binding cleft. TMs 1−7 are labeled for reference. (C and D) Close-up view showing the pose for (C) **10a** and (D) **10b** in the $A_{2A}R$ binding site residues. The residues and compounds are shown in stick models. The residues involved in ligand binding are labeled and represented as violet sticks, oxygen atoms are shown in red, nitrogen atoms are shown in navy blue, and hydrogen atoms are shown in gray. The compounds are represented as purple sticks, the fluorine atom is represented in cyan, and the rest of the indicated atoms are similar to $A_{2A}R$ residues. The dashed lines in black indicate hydrogen bonds.

the active site residue Asn253 and a $\pi-\pi$ stacking interaction with Phe168 of $A_{2A}R$. The exocyclic free amino group of the pyrimidine ring structure of the tricyclic core and the oxygen of the furan ring make strong H-bond interactions with Asn253 of the receptor. This finding is consistent with the results from site-directed mutagenesis studies of the $A_{2A}R$, which suggest that this amino acid is critical for ligand binding.[50] Moreover, the $\pi-\pi$ stacking interaction between Phe168 and His250 stabilizes the binding pose of the compound within the active site. Compound **8** derivatives, including the $A_{2A}R$-bound crystal structure, **17**, are oriented perpendicular to the plane of the cell membrane, with their flexible hydrocarbon side chain located in the extracellular domain. An analysis of ligand-bound crystal structure and literature evidence[47,51] suggests that ECL2 helps in ligand binding at the $A_{2A}R$. We explored the impact of structural variability at the terminal phenolic position of **8** in the GOLD docking scores. As reported previously,[47,51] conformational flexibility was also noted in our experiment; the terminal phenolic side chain forms a polar interaction with a crystallographic water molecule at the extracellular matrix of $A_{2A}R$. As expected, N^6-cyclopentyl-N^8-isopropyl-$N^{8,9}$-dimethyl-9H-purine-6,8-diamine **18** (LUF5608, sixth compound in Table 1), a high affinity A_1R antagonist and negative-control, yielded a very low docking score due to a lack of hydrogen bond formation with the active site residues of the receptor, further authenticating the findings of the docking study and indirectly

dx.doi.org/10.1021/jm500700y | J. Med. Chem. 2014, 57, 6765−6780

Scheme 1. Synthesis of Fluoroalkyltosylates[a]

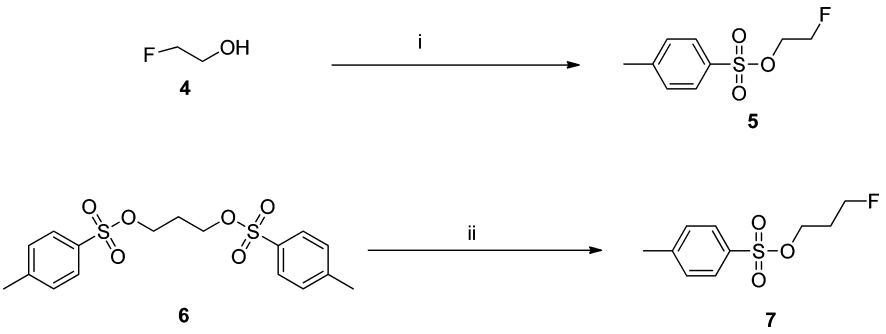

[a]Reagents and conditions: (i) tosyl chloride, pyridine, DCM, room temperature (RT), stirring 3 h; (ii) tetrabutyl ammonium fluoride trihydrate, acetonitrile, overnight reflux.

Scheme 2. Disconnection Retrosynthetic Scheme for the Reference Fluoroalkylated Compound 8 Analogs (10a and 10b)[a]

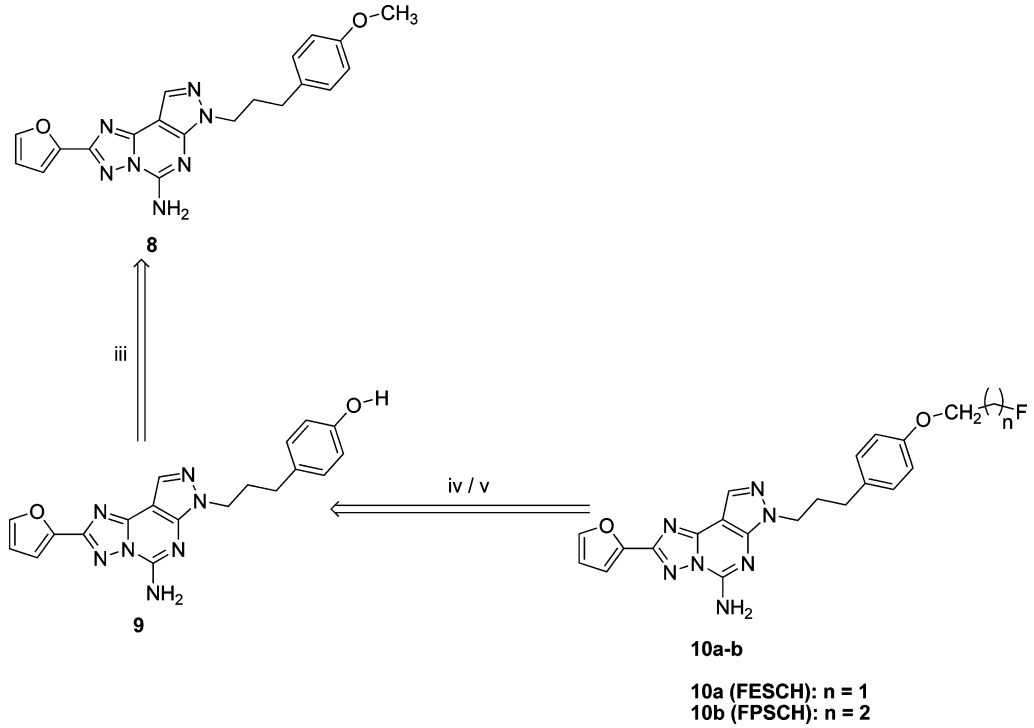

[a]Reagents and conditions: (iii) BBr_3, CH_2Cl_2, RT, 2 h; (iv) **5**, Cs_2CO_3, MeOH, reflux, 1 h; and (v) **7**, Cs_2CO_3, MeOH, reflux, 16 h.

confirming the specificity of **10b** and **10a** toward $A_{2A}R$ over A_1R.

Chemical and Radiochemical Synthesis. The demethylation of commercially available **8** using boron tribromide (BBr_3) resulted in a quantitative yield of 4-(3-(5-amino-2-(furan-2-yl)-7*H*-pyrazolo[4,3-*e*][1,2,4]triazolo[1,5-*c*]pyrimidin-7-yl)propyl)phenol, **9** (precursor of compound **8**, Scheme 2).[47] A retrosynthetic approach was adopted for the synthesis of reference standards (**10a** and **10b**, Scheme 2), which were prepared by reacting the phenol precursor (**9**) with the appropriate fluoroalkyltosylate (**5** or **7** in Scheme 1, selective fluoroalkyaltion) in 35% and 25% yields, respectively. It was adopted for the synthesis of reference standards (**10a** and **10b**, Scheme 2). The two radiolabeled analogs, [^{18}**F**]-**10a** and [^{18}**F**]-**10b**, were synthesized by a two-step two-pot procedure starting with the corresponding [^{18}F]fluoroalkyl synthon ([^{18}**F**]-**5** or [^{18}**F**]-**7**) made from [^{18}F]fluoride and the appropriate ditosylate precursor (**6** or **11**), followed by the selective [^{18}F]fluoroalkylation of the phenol precursor **9** (Scheme 3). Table 2 lists the decay-corrected radiochemical yields, specific radioactivities, calculated partition coefficient (clogP) and experimentally determined distribution coefficient ($LogD_{7.4}$) values for [^{18}**F**]-**10a** and [^{18}**F**]-**10b**. For both tracers, the radiochemical purity was >98%, and the total synthesis time, including quality control, was 114 ± 5 min (n = 18). The identities of the tracers were confirmed by spiking with authentic cold compounds in reversed-phase HPLC (RP-HPLC).

Ligand Metabolism. *In Silico Metabolite Analysis.* The predicted sites of metabolism are highlighted for parent compound **10b** in Scheme 4 (data not shown for **10a** and **8**). The possible metabolic routes can be ranked in the following order: C-hydroxylation > N-oxidation > O-dealkylation.

Human Liver Microsomal Metabolite Analysis. Table 3 summarizes the modifications that were detected with an

dx.doi.org/10.1021/jm500700y | J. Med. Chem. 2014, 57, 6765−6780

Scheme 3. Radiosynthesis of [^{18}F]-10b and [^{18}F]-10a[a]

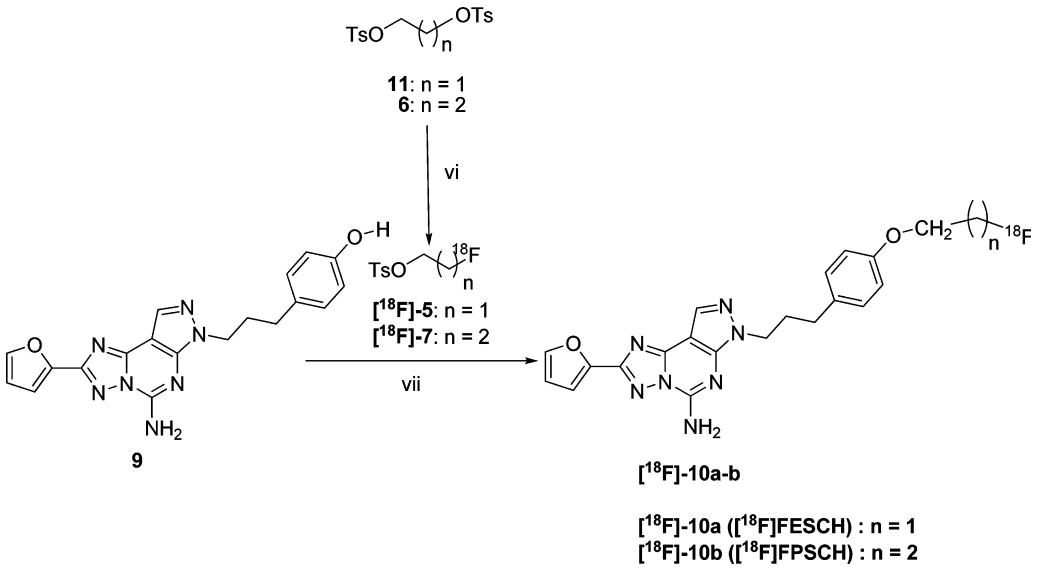

[a]Reagents and conditions: (vi) K[^{18}F]F–$K_{2.2.2}$–K_2CO_3, acetonitrile, **6**, 1,2-ethanediol di-*p*-tosylate, 125 °C, 10 min; (vii) tetrabutyl ammonium hydroxide (40% aq.), acetonitrile, sealed conditions, 115 °C, 15 min.

Table 2. Radiosynthesis and Lipophilicity Data

			clogP		
radioligand	radiochemical yield[a] and purity (%)	specific radioactivity (GBq /μmol)	Chemsketch 12.01	Chembiodraw ultra 12.0	$LogD_{7.4}$[b]
[^{18}F]-**10a**	7 ± 2 and ≥98	22.5 ± 5	2.98 ± 0.98	3.18	3.16 ± 0.03
[^{18}F]-**10b**	8 ± 2 and ≥98	136 ± 13	3.27 ± 0.98	3.41	3.41 ± 0.11

[a]Overall radiochemical yields based on starting wet [^{18}F]fluoride and corrected for decay. [b]Experimental value.

Scheme 4. Sites of Metabolism Predicted for 10b by SMARTCyp Webservice[a]

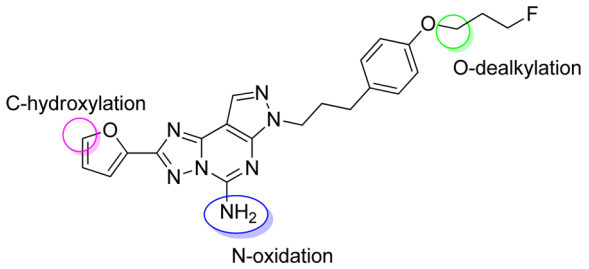

[a]The same predicted metabolic sites are also applicable to compounds **8** and **10a**.

ultrahigh-performance liquid chromatography/quadrupole-time-of-flight-mass spectrometer (UHPLC/Q-ToF-MS) and analyzed by Metabolynx after incubating compound **8** with human liver microsomes. The relative production of the different metabolites over time is presented in Figure 3. None of these modifications and major demethylated metabolites were detected in negative control and positive control (verapamil) incubations, respectively, with human liver microsomes. Under these conditions, the *m*/*z* ratio increased by 16, which is most likely the result of *N*-oxidation or *C*-hydroxylation. The *m*/*z* ratio also decreased by 14, which may be due to a demethylation reaction. Moreover, a fluorine-containing metabolite of **10b** and free fluoride was observed, indicating defluorination, similar to previously reported results for **10a**.[47]

In Vitro Ligand Stability Test. The in vitro stability of the two [^{18}F]tracers ([^{18}F]-**10a** and [^{18}F]-**10b**, Scheme 3) in different solutions such as PBS, saline, rat plasma, and human plasma was determined at 37 °C. After 1 and 2 h of incubation, radio-TLC analysis showed that 95–97% of both tracers were still intact, except in the saline solution. In the saline solution, multiple spots were observed as detected by radio-TLC for both tracers, and the radioactivity corresponding to the intact tracers was only 85–90%.

In Vitro Autoradiographic Experiments. Figure 4 shows autoradiographic images of frozen rat brain sections that were incubated with [^{18}F]-**10a** and [^{18}F]-**10b**. In control sections, a clear difference was noted between the receptor-rich striatum and the receptor-poor cerebellum. The mean striatum-to-cerebellum ratios were 2.75 ± 0.12 ([^{18}F]-**10a**) and 2.99 ± 0.16 ([^{18}F]-**10b**). In the presence of an excess (2 μM) of the A_{2A}R-specific antagonist 8-[(1*E*)-2-(2-(3,4-dimethoxyphenyl)-ethenyl]-1,3-diethyl-3,7-dihydro-7-methyl-1*H*-purine-2,6-dione, **12** (KW6002 in Figure 1), the binding of the tracer to the striatum was strongly reduced and the striatum-to-cerebellum ratio decreased to unity (*n* = 3). Specific binding, as assessed by a blocking study, was 57–62% and 64–67% of the total uptake in the striatum of [^{18}F]-**10a** and [^{18}F]-**10b**, respectively.

Micro PET Images. PET images acquired after injection of [^{18}F]-**10a** and [^{18}F]-**10b** are presented in Figure 5. The two radioligands displayed similar regional distributions that corresponded to the known regional A_{2A}R densities in the rat brain.[7−9,11] In order to prove specific binding, we have used vehicle-control and blocker animals (Please refer in vivo and in vitro selectivity of the experimental section for more details). In

dx.doi.org/10.1021/jm500700y | J. Med. Chem. 2014, 57, 6765−6780

Table 3. Human Liver Microsomal Metabolite Analysis

Chemical Structure	Mass modification	Rt (Min)	Mass of metabolite	Proposed fragment loss or addition from / to parent
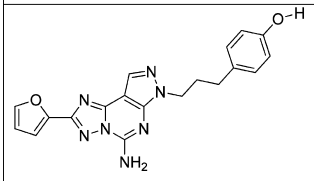	-14.01	2.52	375.14	$-CH_2$
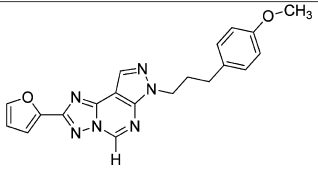	-15.01	2.53	376.12	-NH (Deamination)
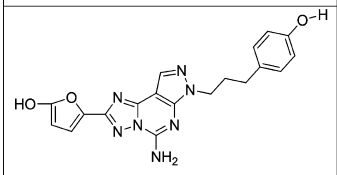	1.98	2.07	391.13	$-CH_2$ & +O (Demethylation + C-hydroxylation)
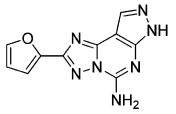	-148.08	1.78	241.07	$-C_{10}H_{12}O$ (Parent-$C_{10}H_{12}O$)
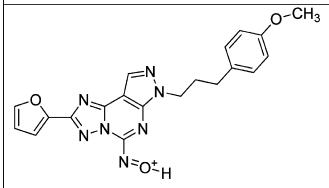	+15.99	2.44	405.15	+O (N-Oxidation or C-hydroxylation)

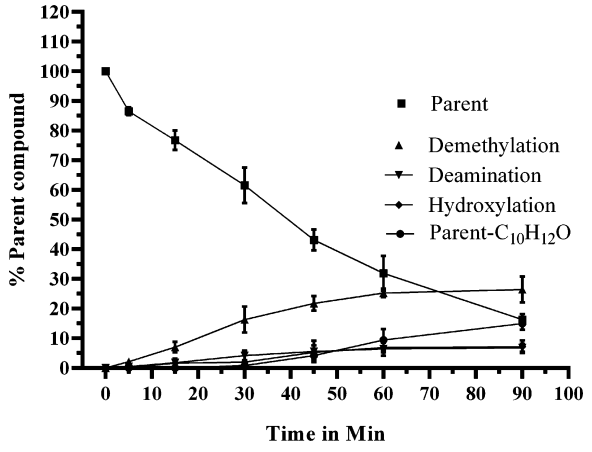

Figure 3. Relative amounts of several modifications over 90 min during incubation of (**8**) with human liver microsomes. The error bars indicate the standard deviation.

vehicle-control animals, the striatum was clearly visualized. The extrastriatal binding of both tracers was hardly visible, but strong uptake was observed in the skull bone. When animals were pretreated with the $A_{2A}R$ antagonist **12** (1 mg/kg), the cerebral uptake of the tracers was strongly reduced, and regional differences in tracer uptake were no longer observed.

In Vivo Radioligand Kinetics and Metabolism. *Kinetics of Radioactivity in Brain.* The cerebral kinetics of radioactivity after the injection of [^{18}F]-**10a** and [^{18}F]-**10b** are presented in Figure 6 (panels A–D). In vehicle-treated control animals (n = 6), the uptake of radioactivity rapidly increased to a maximum (2.5 min after injection), which was followed by an exponential washout (panels A and C). In animals treated with **12** (n = 6), the cerebral uptake of ^{18}F was strongly reduced, and the radioactivity was rapidly washed out from all brain regions (panels B and D). The difference in the striatal uptake of ^{18}F in control and pretreated rats was statistically significant at most time points.

We estimate receptor occupancy on the basis of PET-standardized uptake values (PET-SUVs) (at the time of maximum uptake), reported $A_{2A}R$ densities (953 fmol/mg protein in rat striatum[52]) and injected tracer doses in nanomolar amounts. Assuming that brain tissue contains 10% protein, we calculated that less than 2% and 8% of the cerebral $A_{2A}R$ population was occupied by [^{18}F]-**10b** and [^{18}F]-**10a**, respectively, in both control- and blocker-treated rats.

Radioactivity Kinetics in Plasma. A rapid, biexponential plasma clearance was observed in all groups. Pretreatment did

dx.doi.org/10.1021/jm500700y | J. Med. Chem. 2014, 57, 6765–6780

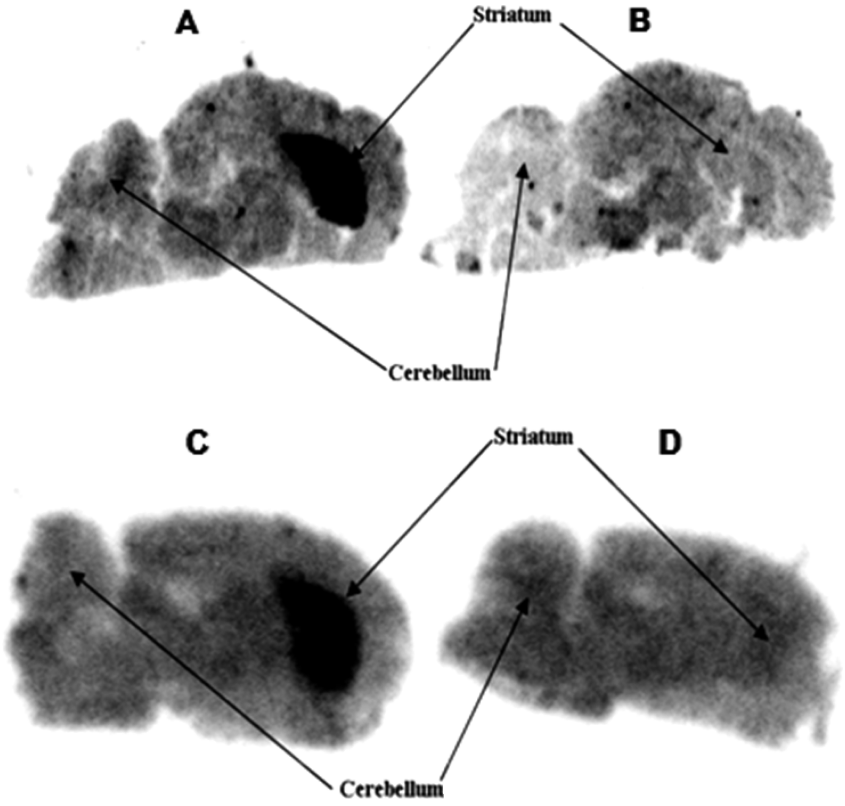

Figure 4. Autoradiographic images of sagittal sections of rat brains after 90 min of incubation with (A and B) [^{18}F]-**10b** or (C and D) [^{18}F]-**10a** in the (B and D) presence or (A and C) absence of an excess of a known A_{2A}R-selective antagonist, **12** (2 μM).

not significantly affect the clearance of radioactivity from the plasma compartment.

In Vivo Metabolite Analysis. An unidentified radiometabolite with a R_f value of 0−0.1 was observed in rat plasma (the R_f value of authentic [^{18}F]-**10b** was 0.6). The fraction of total plasma radioactivity representing the parent compound decreased to 66 ± 16% at 60 min and 53 ± 20% at 90 min. Pretreatment with **12** did not affect the rate of tracer metabolism. The fraction of total plasma radioactivity representing [^{18}F]-**10a** was 46 ± 17% at 60 min and 36 ± 14% at 90 min.

Ex Vivo Biodistribution Data. The biodistribution data for both tracers are shown in Figure 7. After pretreatment with **12**, the uptake of both compounds was reduced in the A_{2A}R-rich striatum (approximately 69% of [^{18}F]-**10b** and 45% for [^{18}F]-**10a**). For [^{18}F]-**10b**, the effect of the blocker was statistically significant in the frontal cortex and striatum, whereas for [^{18}F]-**10a** (n = 3), no significant effect of the blocker was observed in any of the brain regions; however, the greatest decrease of the tracer uptake was observed in the striatum. Striatum-to-cerebellum ratios can be used as indices for the in vivo binding of the tracers to A_{2A}Rs. Striatum-to-cerebellum ratios of 3.5 and 2.1 were reached at 106 min postinjection for [^{18}F]-**10b** (n = 6) and [^{18}F]-**10a** (n = 3), respectively. The ratios of the uptake in other regions to the cerebellum were approximately equal to one. The standard uptake values in the skull bone (2.06 ± 0.58) for [^{18}F]-**10b** were significantly higher than those of [^{18}F]-**10a** (0.29 ± 0.05).

For both tracers, the plasma-to-blood ratio was greater than one, and the negligible binding to red blood cells in pretreated and control animals indicated that the radioligands preferentially distributed to the plasma.

DISCUSSION

We have evaluated [^{18}F]-**10a** and [^{18}F]-**10b** as PET tracers for the cerebral imaging of A_{2A}Rs; these tracers may provide many logistic advantages and can be used in centers without an on-site cyclotron. Thus, we synthesized fluorinated molecules based on a pyrazolo-triazolo-pyrimidine template (compound **8**) that is known to cross the BBB because of its appropriate lipophilicity (clogP = 2.9), molecular weight, charge, and hydrogen bonding.[39,43,44] The molecular docking approach provides valuable atomic-level insight into the behavior of a small molecule in the binding site of the protein. It also provided insight into the binding mode of compound **8** derivatives to the active site of the receptor. Compound **8** and its fluoro analogs (**10a** and **10b**) had better GOLD fitness scores than the clinically studied PET tracer (E)-8-(3,4,5-trimethoxystyryl)-1,3-dimethyl-7-[^{11}C]methylxanthine ([^{11}C]-KF18446) and the A_{2A}R-bound crystal structure **17**. GOLD scores are good indicators to predict the binding orientations of compound **8** derivatives. A higher score predicts better binding orientations with the receptor residues. We have used the A_1R decoy, **18**-as negative control, to validate the quality of the GOLD scoring function.[53] Small structural changes of the phenoxy substituent appeared to be well-tolerated, and this is substantiated by our in vivo study. Subtype selectivity can be expected because the lead compound **8** shows a >10,000-fold selectivity for the A_{2A}R subtype compared to other AR subtypes. Moreover, the binding affinities of **8** (K_i = 0.5 nM) and **10a** (K_i = 12.4 nM) to the A_{2A}R were adequate for imaging.[43,47] Even though the reported K_i value of 53.6 nM for **10b**[54] is much lower than that of the lead compound **8**, the affinity data predict faster clearance than **8** and **10a** and more preferable brain kinetics for the quantitative evaluation of the

dx.doi.org/10.1021/jm500700y | J. Med. Chem. 2014, 57, 6765−6780

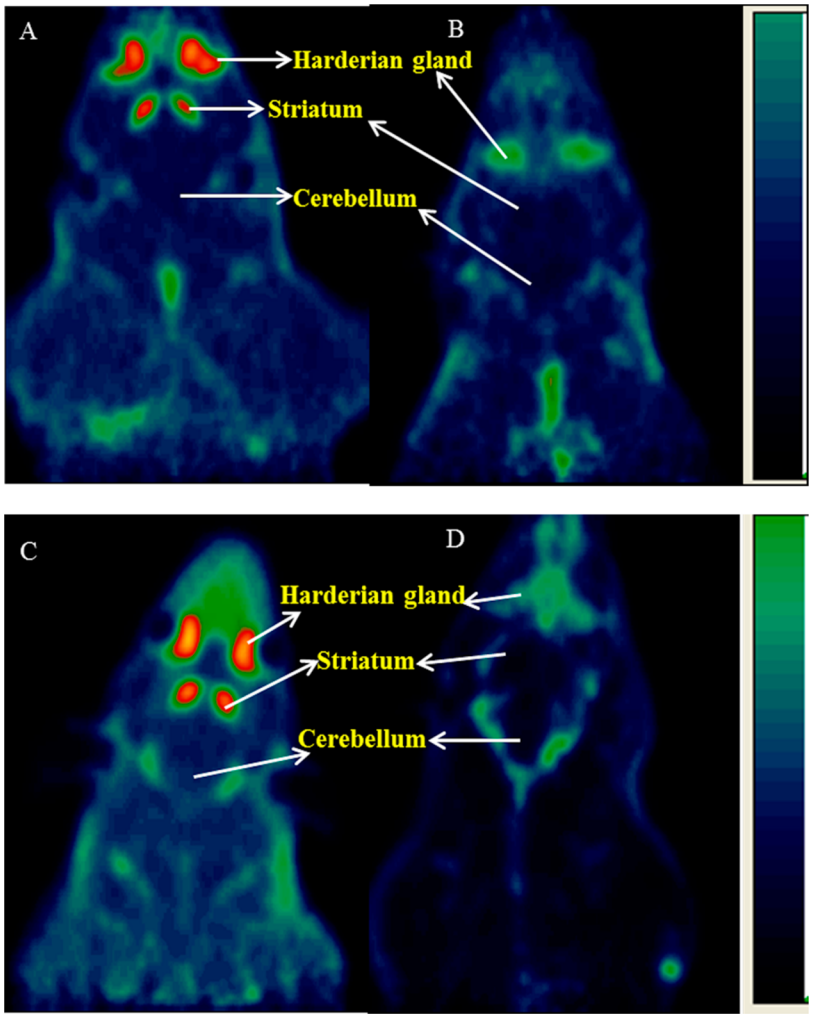

Figure 5. Small-animal PET images of a coronal plane of rat brains after injections of (A and B) [^{18}F]-**10a** or (C and D) [^{18}F]-**10b**. The images represent the summed frames from 17 to 90 min post injection. (A) Vehicle-control (left); (B) a compound **12**-treated animal ([^{18}F]-**10a**) (right). (C) Vehicle-control (left); (D) a compound **12**-treated animal ([^{18}F]-**10b**) (right). The images were normalized for body weight and injected dose.

ligand−receptor binding. The pyrazolo-triazolo-pyrimidine scaffold allows for the easy and quick incorporation of an [^{18}F] label in the acidic phenol group, and this phenoxy substituent can also be used to modify the lipophilicity of the compound. Fluoroalkyl chain lengthening beyond the fluoropropyl substituent results in a higher molecular weight (MW) and lipophilicity for a compound. It has been suggested that the MW should be kept below 450 Da to facilitate brain penetration with fewer side effects such as high rapid metabolic turnover, poor absorption, and toxicity.[55] High lipophilicity causes unacceptable binding to plasma proteins, decreasing the free drug concentration available to pass the BBB, or binding to hydrophobic protein targets other than the desired one, resulting in high levels of nonspecific binding in the brain.[39,55] On the basis of these considerations, **10b** was selected as a novel candidate for radiolabeling to obtain the expected lipophilicity and a MW that ensures the crossing of the BBB.

Computational prediction of the sites of cytochrome *P450* (CYP450)-mediated metabolism and an in vivo plasma radio-TLC metabolite analysis indicated the formation of polar metabolites, which are not expected to cross the BBB. The results obtained after incubation of **10b** with hepatic microsomes were in good agreement with a previously reported experiment and the predictions of a two-dimensional (2D) method (SMARTCyp) describing CYP450-mediated drug metabolism.[47,56] In contrast to the results obtained from a SMARTCyp prediction of drug metabolism (please refer to Ligand Metabolism module in the Results section), the metabolic routes of compound **8** after incubation with liver microsomes can be ranked in the following order: O-dealkylation > parent-$C_{10}H_{12}O$ > N-oxidation or C-hydroxylation > deamination (Figure 3, Table 3). A stability test indicated that both **10a** and **10b** are highly stable in vitro. Because of the observed multiple spots as detected with radio-TLC in a saline solution, we used PBS instead of saline in the formulation of the tracers. The fraction of total plasma radioactivity representing [^{18}F]-**10b** was 18−20% higher than that of [^{18}F]-**10a** at both 60 and 90 min in our in vivo metabolite analysis. However, stronger skull bone radioactivity uptake (i.e., stronger defluorination) was observed with [^{18}F]-**10b** than [^{18}F]-**10a** in both an ex vivo biodistribution study and a small-animal PET (microPET) image analysis. In our imaging studies (especially with [^{18}F]-**10b**), the accurate quantitation of the radioactivity in the frontal cortex was difficult due to spillover from radiofluorine in the skull bone.

A retrosynthetic approach for **10a** and **10b** synthesis was successfully applied to avoid a cumbersome and time-

dx.doi.org/10.1021/jm500700y | J. Med. Chem. 2014, 57, 6765−6780

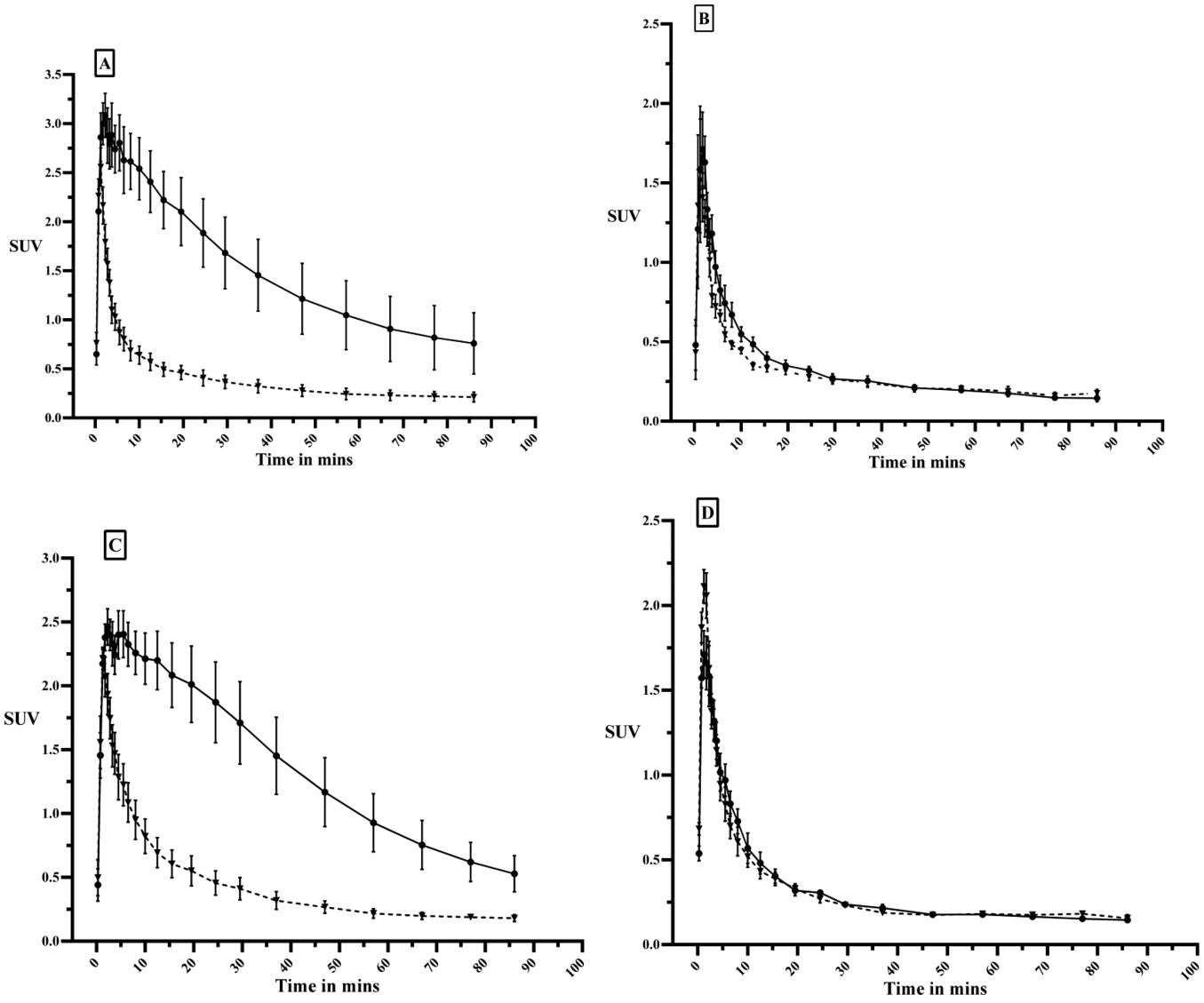

Figure 6. (A–D) Kinetics of (A and B) [^{18}F]-**10a** and (C and D) [^{18}F]-**10b**-derived radioactivity in the rat brain. The error bars indicate the SEM. (A and C) Vehicle-control animals (left); (B and D) compound **12**-treated animals (right). ●, striatum; ▼, cerebellum.

consuming scheme involving 8 reaction steps. In the synthesis of compound **10b**, 3-fluoropropyl tosylate **7** yielded a slightly better result than 1-bromo-3-fluoropropane (25% vs 19% yield) because tosylate is a better leaving group than bromide. Tracers were successfully synthesized using a two-pot two-step procedure (Scheme 3). The [^{18}F]fluoroalkylation of phenol precursor **9** using corresponding intermediate fluorosynthons ([^{18}F]-**5** or [^{18}F]-7) yielded the desired ligands [^{18}F]-**10a** and [^{18}F]-**10b** at moderate yields (7–8%) and satisfactory specific activities (Table 2). The average radiochemical yield of the [^{18}F]-**5** or [^{18}F]-7 obtained was 50 ± 5%, whereas the final fluoroalkylation conversion was approximately 25 ± 5%. Purification by HPLC and solid phase extraction provided a decay-corrected radiochemical yield of 7–8%. The long evaporation step of the captured eluate [14 mL of hexane/ether (3:1)] during the purification of the [^{18}F]-**5** or [^{18}F]-7 and the losses that occurred during the other manipulations of the synthesis accounted for the moderate radiochemical yields of the synthesized tracers [^{18}F]-**10a** and [^{18}F]-**10b.** The purification of the [^{18}F]-**5** or [^{18}F]-7 by RP-HPLC and C-18 light Sep-Pak columns may improve the radiochemical yield. Our radiosynthetic procedure for [^{18}F]-**10a** is much faster (by 15–20 min) than the existing procedure.[47] The applied radiolabeling approach is versatile; we can quickly adopt the same procedure for the radiosynthesis of both compounds [^{18}F]-**10a** and [^{18}F]-**10b**. The radiochemical purities were also adequate and amounted to more than 98% of the total radioactivity as determined by UHPLC quality control.

In vitro autoradiography (ARG) confirmed the selectivity of [^{18}F]-**10a** and [^{18}F]-**10b** for A_{2A} Rs. The tracer binding pattern, especially in the striatum and other parts of the brain, was comparable with ex vivo biodistribution readings. The regional distribution of radioactivity in the rat brain after the injection of [^{18}F]-**10a** and [^{18}F]-**10b** also suggests that these tracers are capable of measuring regional A_{2A}R densities. After pretreatment with a subtype-selective xanthine antagonist, **12**, the tracer uptake in the striatum was greatly suppressed, and regional differences were no longer present. In the biodistribution and PET studies, the uptake of [^{18}F]-**10b** in the cerebellum and frontal cortex (areas lacking A_{2A}Rs) was also decreased after pretreatment with **12**. The most logical explanation for the specific binding in the cerebellum is that

dx.doi.org/10.1021/jm500700y | J. Med. Chem. 2014, 57, 6765–6780

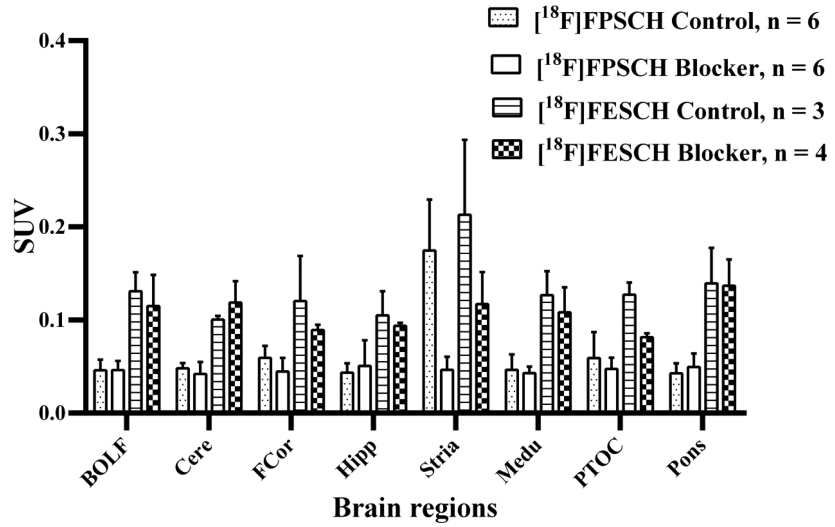

Figure 7. Cerebral biodistribution data of [^{18}F]-**10b** and [^{18}F]-**10a** at 106 min after injection. The error bars indicate the SEM. BOLF = Bulbus olfactorius, CERE = Cerebellum, FCor = Frontal cortex, Stria = Striatum, Hipp = Hippocampus, Medu = Medulla, PTOC = Parietal/Temporal/Occipital Cortex.

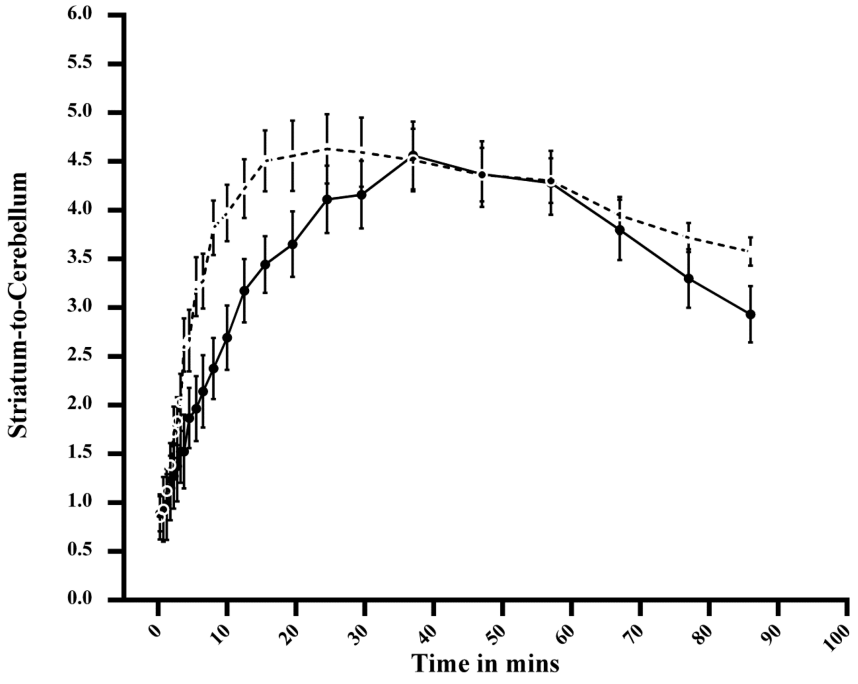

Figure 8. Striatum-to-cerebellum ratios of [^{18}F]-**10b** and [^{18}F]-**10a** as a function of time. The solid and broken lines represent [^{18}F]-**10b** and [^{18}F]-**10a**, respectively. The error bars indicate the SEM.

the endothelium and blood vessels express A_{2A}Rs, even if the brain tissue does not.[18,57] Taking into account the findings that pretreatment with **12** reduces the distribution volume of candidate reference tissues such as the cerebellum, we choose not to quantify the blocking effect using a (simplified) reference tissue model, 2-tissue compartment model, and Logan analysis.

It is evident from the microPET images that the extrastriatal binding of the [^{18}F]-tracers was barely visible, except for the strong uptake in skull bone due to defluorination, whereas in the case of xanthine PET ligands, the extrastriatal retention of radioactivity was visualized in the cortex, cerebellum, and thalamus.[34] Because of estimated receptor binding of the injected tracer mass (<2%−8%), we do not expect any pharmacological effects or change in the physiological states of the A_{2A}R system during our microPET study.

The striatal uptake of both [^{18}F]-ligands was clearly visualized using PET scans; both tracers reached a striatum-to-cerebellum ratio of approximately 4.6, which is similar to the experiments with [^{11}C]-**8** result (4.6 ± 0.27).[44] However, the maximum ratio for [^{18}F]-**10b** was reached at a later time point (37 min) than that of [^{18}F]-**10a** (25 min) and [^{11}C]-**8** (15 min), most likely because of the higher lipophilicity of [^{18}F]-**10b** (Figure 8). Lipophilicity may prolong the circulating half-life of a tracer, resulting in extended availability for binding to A_{2A}Rs. After the maximum had been reached, the concentration of [^{18}F]-**10a** in the brain remained fairly stable until 30 min after injection (similar to [^{11}C]-**8**), whereas the concentration

dx.doi.org/10.1021/jm500700y | J. Med. Chem. 2014, 57, 6765−6780

of [^{18}F]-**10b** showed a somewhat stronger washout. The cerebral kinetics of both radioligands were compatible with the duration of a PET scan (Figure 8).

CONCLUSION

[^{18}F]-**10b** and [^{18}F]-**10a** could be prepared using a two-step procedure. Both radioligands showed a distribution in the rat brain, corresponding to the regional A_{2A}R densities known from in vitro ARG and binding assays. Experimental $LogD_{7.4}$ values, plasma metabolite analysis and microPET data analysis results suggest that these radiopharmaceuticals are potentially useful for mapping cerebral A_{2A}Rs. The molecular docking studies, similar target-to-nontarget ratios in ex vivo brain biodistribution and kinetic analysis, distribution patterns and only slightly different kinetics suggest that small increases in the length of the fluoroalkyl chain do not result in impaired pharmacokinetics and metabolic stability.

EXPERIMENTAL SECTION

In silico Docking Studies. The coordinates of the X-ray crystal structure of human A_{2A}R in complex with the triazolotriazine **17**, a high-affinity and selective A_{2A} antagonist (Figure 2, protein data bank ID: 3PWH, www.rcsb.org/pdb), plus those of some well-known A_{2A}R antagonists, were used as a basis for ligand docking to investigate the binding properties of **10a** and **10b** (Figure 2, panel **B** and **C**). The three-dimensional (3D) structures of these molecules were drawn using the SYBYL 7.1 molecular modeling package.[58] Next, the constructed molecules were energy minimized using the Powell method for 10000 iterations with 0.05 kcal/mol as a gradient.[59] A tripos force field and Gasteiger-Hückel charges were used during minimization.[60] The GOLD 5.1 docking protocol was employed for the analysis.[61] Hydrogens were added to the crystal structure, and a grid of size 10 Å was constructed around the cocrystallized ligand. The cocrystallized ligand was removed after the preparation of the grid. The docking was then carried out to predict the binding mode of the same cocrystallized ligand, and a comparison was made with the crystallographically observed positions (n = 3). Compound **18**, a high affinity A_1R antagonist was included as a decoy compound in a pool of known A_{2A}R antagonists to further validate the docking protocol. The GOLD fitness score and the various interactions, such as hydrogen bonding/$\pi-\pi$ interactions with important active site residues from the validated docking protocol, were selected as evaluation criteria. The docking poses were analyzed using Pymol (Delano Scientific LLC, San Carlos, CA).

Materials (Chemical Synthesis). The compounds **8** and **12** were purchased from Axon Medchem BV (Groningen, The Netherlands). 1,3-Propanediol di-*p*-tosylate (**6**) and 1,2-ethanediol di-*p*-tosylate (**11**) were procured from Aldrich (Sigma-Aldrich, The Netherlands). Tetrabutylammonium hydroxide solution (40% in H_2O) was purchased from Fluka (Sigma-Aldrich, The Netherlands). All other chemicals were of analytical grade and obtained from commercial suppliers such as Rathburn, Sigma, Merck, and others. These chemicals were used in the syntheses without any further purification. Oxygen- or moisture-sensitive reactions were carried out under an atmosphere of dry N_2 or argon using dried glassware.

Methods for Chemical Synthesis and Molecular Characterization. Nuclear magnetic resonance spectra were recorded on a Bruker Avance 500 spectrometer [(^{1}H NMR (500 MHz), ^{13}C NMR (125 MHz)], or a Varian Oxford 400 MHz spectrometer [^{1}H NMR (400 MHz), ^{13}C NMR (100 MHz)]. Chemical shifts are reported as δ values and coupling constants are presented in hertz (Hz). Chemical shifts for ^{13}C NMR spectra are reported in ppm relative to the solvent peak.

UHPLC-HRMS was used to assess the exact molecular weight of the reference compounds ([^{18}F]-**10a** and [^{18}F]-**10b**) and intermediate fluorosynthons ([^{18}F]-**5** and [^{18}F]-**7**). The HPLC method was used to calculate the purity of the compounds. Purities of all compounds were found to be ≥95%. A sample solution (100% acetonitrile) with a concentration of approximately 0.1 mg/mL was prepared, and an injection volume of 5 μL was used. Data were acquired as described in the in vitro microsomal metabolite analysis section using a 4 min gradient starting from 0.1% formic acid in 95% water for 1.5 min, next with an 80% acetonitrile solution for 1 min, and finally with 0.1% formic acid in 95% water at a flow rate of 0.6 mL/min.

A disconnection retrosynthetic strategy was designed for the easy preparation of the **10a** and **10b** analogues.[47,54] Compound **8**, in dichloromethane (DCM) was demethylated using BBr_3; this yielded the precursor **9**. This precursor was used without further purification for both the chemical and radiochemical syntheses.

Precursor **9** was characterized by ESI-HRMS m/z 376.1522 [M + H]$^+$, $C_{19}H_{17}N_7O_2$.H+: Calcd 376.1522; ^{1}H NMR (400 MHz, Methanol-d_4): δ 8.08 (s, 1H), 7.78 (dd, J = 1.7, 0.7 Hz, 1H), 7.30 (dd, J = 3.5, 0.7 Hz, 1H), 6.92−6.83 (m, 2H), 6.66 (dd, J = 3.6, 1.8 Hz, 1H), 6.60−6.50 (m, 2H), 4.28 (t, J = 6.9 Hz, 2H), 2.47 (t, J = 7.5 Hz, 2H), 2.26−1.96 (m, 2H).

*2-[^{19}F]-Fluoroethyl Tosylate (**5**).* 2-Fluoroethanol **4** (1.28 g, 20 mmol) was dissolved in 20 mL of DCM at 0 °C. Tosyl chloride (4.19 g, 22 mmol) and pyridine (1.74 g, 22 mmol) were added to this solution. The reaction mixture was then allowed to warm to room temperature and stirred continuously for 3 h. After the addition of water (100 mL) and saturated ammonium chloride solution (50 mL), the mixture was extracted with DCM (3 × 150 mL). The combined organic fractions were washed thoroughly with brine, dried over anhydrous sodium sulfate, and concentrated in vacuo to generate the crude product. The crude product was then purified by silica column purification using *n*-hexane:DCM (50% v/v) as an eluent to generate pure **5** (Scheme 1) in the form of colorless oil, R_f 0.34. The isolated yield was 51%.

ESI-HRMS m/z 241.0309 [M + Na]$^+$, $C_9H_{11}O_3FS.Na^+$: calcd 241.0310; ^{1}H NMR (400 MHz, $CDCl_3$): δ 7.80 (d, J = 8.3 Hz, 2H), 7.35 (d, J = 8.3 Hz, 2H), 4.62 (dd, J = 5.0, 3.2 Hz, 1H), 4.50 (dd, J = 5.0, 3.2 Hz, 1H), 4.29 (dd, J = 4.9, 3.3 Hz, 1H), 4.22 (dd, J = 4.9, 3.3 Hz, 1H), 2.44 (s, 3H).

*3-[^{19}F]-Fluoropropyl Tosylate (**7**).* Tetrabutyl ammonium fluoride trihydrate (52.8 mg, 0.20 mmol) was dried azeotropically with 3 × 3 mL acetonitrile. During coevaporation, care should be taken to ensure that the temperature of the flask does not rise above 30 °C to prevent the decomposition of the tetrabutyl ammonium fluoride trihydrate. The contents of the flask were redissolved in a small amount of anhydrous acetonitrile, and this solution was added to a refluxing solution of 1, 3-propanediol di-*p*-tosylate **6** (76.9 mg, 0.2 mmol) in acetonitrile. The reaction progress was monitored by TLC on silica plates [DCM: hexane (1.25:1 v/v)]. The refluxing was continued overnight with stirring. The obtained solution was filtered, and the filtrate was evaporated under reduced pressure. The residue was redissolved in a small amount of mobile phase and purified using silica gel column chromatography with a mixture of DCM and hexane (50%) as the eluent to yield pure **7** (Scheme 1) in the form of a clear, slightly yellowish oil.

ESI-HRMS m/z 213.0583 [M − F]$^+$, [$C_{10}H_{13}O_3S$−F]$^+$: calcd 213.0585; high in-source fragmentation; ^{1}H NMR (400 MHz, $CDCl_3$): δ = 7.80 (d, J = 8.2, 2H), 7.35 (d, J = 8.1, 2H), 4.54 (t, J = 5.7, 1H), 4.45 (t, J = 5.6, 1H), 4.16 (t, J = 6.2, 2H), 2.45 (s, 3H), 2.14−1.94 (m, 2H).

*7-(3-(4-(2-Fluoroethoxy)phenyl)propyl)-2-(furan-2-yl)-7H-pyrazolo[4,3-e][1,2,4]triazolo [1,5-c]pyrimidin-5-amine (**10a**).* The synthesis of this compound was performed according to a published procedure. The authenticity of the **10a** (Scheme 2) was confirmed by ^{1}H NMR, ^{13}C NMR, and MS data and was in agreement with the published values.[47]

*7-(3-(4-(3-Fluoropropoxy)phenyl)propyl)-2-(furan-2-yl)-7H-pyrazolo[4,3-e][1,2,4]triazolo[1,5-c]pyrimidin-5-amine (**10b**).* The selective fluoropropylation reaction described in the literature was slightly modified to generate authentic nonradioactive **10b** (Scheme 2).[54] Our procedure differed in the fluoroalkylating agent; we used **7** instead of 1-bromo-3-fluoropropane.

dx.doi.org/10.1021/jm500700y | J. Med. Chem. 2014, 57, 6765−6780

The phenol precursor **9** was dried azeotropically with 3 × 8 mL anhydrous toluene and then suspended in anhydrous MeOH (3 mL), and Cs_2CO_3 (110 mg, 0.34 mmol) and 3-fluoropropyltosylate **7** (79 mg, 0.34 mmol) were added. The reaction mixture was refluxed for 16 h with continuous stirring. The conversion was monitored by TLC (14% acetonitrile in chloroform). The crude mixture was then concentrated in vacuo, and the crude product was redissolved and purified by preparative TLC with 14% acetonitrile in chloroform as a mobile phase to furnish 7.9 mg of product. The product was contaminated with trace silica gel. To remove the silica gel impurities, the sample was redissolved in the mobile phase, passed through a 0.45 μm polytetrafluoroethylene (PTFE) syringe filter, and concentrated to provide 7.4 mg (25%) of **10b** (Scheme 2) as a white solid.

ESI-HRMS *m/z* 436.1899 $[M + H]^+$, $C_{22}H_{22}N_7O_2F.H+$: calcd 436.1897; ^{1}H NMR (500 MHz, $CDCl_3$): δ 8.24 (s, 1H), 7.67 (s, 1H), 7.29 (d, *J* = 5.8 Hz, 2H), 7.12 (d, *J* = 8.0 Hz, 2H), 6.83 (d, *J* = 8.1 Hz, 2H), 6.64 (s, 1H), 5.98 (s, 2H), 4.70 (t, *J* = 5.6 Hz, 1H), 4.61 (t, *J* = 5.5 Hz, 1H), 4.40 (t, *J* = 6.7 Hz, 1H), 4.08 (t, *J* = 5.9 Hz, 1H), 2.64 (t, *J* = 7.4 Hz, 2H), 2.37−2.04 (m, 4H); ^{13}C NMR (125 MHz, $CDCl_3$): δ 157.08, 149.15, 147.83, 145.49, 144.87, 144.64, 133.26, 132.03, 129.38, 114.40, 112.74, 112.04, 97.26, 81.47, 80.16, 63.53, 46.97, 31.98, 31.19, 30.53, 30.38, 29.71.

Radiochemistry. [^{18}F]-**10a** and [^{18}F]-**10b** were prepared by a two-pot radiosynthetic method, using the intermediate fluorosynthons [^{18}F]-**5** and [^{18}F]-**7** (Scheme 3, Table 2).

No-carrier added aqueous [^{18}F] fluoride was produced by the irradiation of [^{18}O] water via the ^{18}O (p,n) ^{18}F nuclear reaction using a Scanditronix MC-17 biomedical cyclotron. The [^{18}F] fluoride solution from the target was trapped onto a preactivated Sep-Pak light Accel plus QMA anion-exchange cartridge to recover the ^{18}O-enriched water. The [^{18}F]fluoride was then eluted from the column with 1 mL of potassium carbonate solution (1 mg/mL) into a glass conical vial containing 15 mg of Kryptofix [2.2.2]. To this mixture, 1 mL of acetonitrile (Rathburn, The Netherlands) was added, and the solvents were evaporated to dryness azeotropically at 130 °C. The [^{18}F]KF/Kryptofix [2.2.2] complex was dried 3 times by the addition of 0.5 mL acetonitrile, and the solvent mixture was evaporated.

A solution of **6** or 1,2-ethanediol di-*p*-tosylate **11** (4−5 mg) in acetonitrile (0.5 mL) was added to the conical vial, and the vial was heated on a heating block to 125 °C for 10 min under sealed conditions and then cooled to room temperature to generate the crude intermediate. The cooled reaction mixture was diluted with 4 mL hexane/diethyl ether (3:1) and loaded onto a Sep-Pak Silica Plus column (Waters). The cartridge was then eluted with 10 mL of hexane/diethyl ether (3:1), and the eluate captured in a counting vial was evaporated on a rotavap (Buchi HB-140) to obtain the desired pure [^{18}F]fluorosynthon [^{18}F]-**5 or** [^{18}F]-**7**.

Phenol precursor **9** (1.5 mg) in 0.3 mL acetonitrile and 10 μL of 40% aqueous tetrabutylammonium hydroxide solution were added to the residual solution of 3-[^{18}F]-fluoropropyltosylate [^{18}F]-**7** or 2-[^{18}F]-fluoroethyltosylate [^{18}F]-**5**. The reaction vials were closed and maintained at 115 °C for 15 min on a heating block. After cooling to room temperature, the reaction mixture was diluted with 0.6 mL of HPLC mobile phase and injected onto a semipreparative Phenomenex Prodigy ODS C-18 RP-HPLC column (5 μm, 10 × 250 mm) connected to a UV-spectrometer (Waters 486 tunable absorbance detector) set at 254 nm and a Bicron Frisk-Tech radiation detector. The HPLC column was then eluted with 45% acetonitrile and 55% 100 mM ammonium acetate at 5 mL/min to yield [^{18}F]-**10b** (t_R = 16 min); in the case of [^{18}F]-**10a**, the elution solvent was 40% acetonitrile and 60% 100 mM CH_3COONH_4, t_R = 21 min. The collected HPLC fractions containing the products were diluted with water (25 mL) and loaded onto C-18 light Sep Pak cartridges (Waters). After trapping the radioactivity, the columns were washed with an additional 4 mL of water. The columns were dried with a flow of nitrogen and eluted with 1 mL of ethanol over a 0.22 μm Millex LG sterilization filter; the products were collected in a 25 mL sterile vial (Mallinckrodt pharmaceuticals, The Netherlands). The products were diluted with saline (4 mL), and the formulated tracers were submitted for quality control.

Independent quality control was performed on a Waters (Milford, MA) Acquity Ultraperformace LC quaternary solvent manager coupled to a tunable, dual-wavelength Ultraviolet/Visible (UV/vis) detector and a radioactivity detector (Berthold Flowstar LB 513). The radioactive product (10 μL) was injected into a Waters 3.0 × 50 mm i.d., 1.7 μM Ethylene-Bridged Hybrid (BEH) shield RP18 column and eluted using 40% acetonitrile at a flow rate of 0.8 mL/min. The instrument and column temperature were set at 254 nm and 35 °C, respectively. The retention time for [^{18}F]**10b** was 3.2 min, and the retention time for [^{18}F]**10a** was 1.9 min.

Ligand Metabolism. *In Silico Metabolite Analysis.* The SMARTCyp web service (version 2.4.2) was used to predict which sites in the molecule are most vulnerable to CYP450 metabolism.[56] SMARTCyp has been shown to be valid for the metabolism of the major isoforms 1A2, 3A4, 2A6, 2B6, 2C8, 2C19, and 2E1. Additionally, it is applicable to specific models for the 2C9 (CYP2C9) and 2D6 (CYP2D6) isoforms.[56]

SMARTCyp only uses the 2D structure of a compound as input, and atoms are scored based on their propensity to undergo metabolism, which is in turn calculated based on energy and accessibility factors. The energy required for oxidation at each atom is computed by fragment matching toward the SMARTS patterns. The accessibility is approximated as the relative topological distance of an atom from the center of the molecule, and the final score is computed as score = energy − 8 × accessibility.[56]

Human Liver Microsomal Metabolite Analysis. Human liver microsomes (HLM) from 150 mixed-gender donors and a NADPH-regenerating system consisting of two solutions (NADP plus glucose-6-phosphate and glucose-6-phosphate dehydrogenase) were purchased from BD Biosciences. Dulbecco's Phosphate-Buffered Saline (DPBS), pH 7.4, was procured from Life Technologies.

Nonradioactive compounds **8** and **10b** were incubated with HLM. The metabolic reactions were initiated by the addition of NADPH. At different time points (0, 5, 15, 30, 45, 60, and 90 min), 100 μL of the solution was taken. After quenching with cold acetonitrile and centrifugation at 17250*g*, the supernatant solution (5 μL) was injected into a UHPLC/Q-ToF-MS. Incubations without NADPH, microsomes, and test compound were conducted as negative controls to characterize the nonmetabolism related degradation of the test compound. Furthermore, verapamil was included as a positive control because it is known to be metabolized by human liver microsomes. MetaboLynx (Waters) was used to assist in the identification of metabolites.

UHPLC/Q-TOF-MS Method. Data acquisition was performed using Waters (Milford, MA) Acquity Ultraperformace LC quaternary solvent manager. The samples were injected onto a Waters 3.0 × 50 mm internal diameter (i.d.), 1.7 μM BEH shield RP 18 column and eluted using a 6 min gradient starting from 0.1% formic acid in 98% water for 5 min, then with a 100% acetonitrile solution for 0.5 min, and finally with 0.1% formic acid in 98% water at a flow rate of 0.6 mL/min and a column temperature of 35 °C. The mass spectrometer was operated in electrospray positive ionization mode with an extended dynamic range and resolution mode analyzer; the machine settings were 0.5 kV capillary voltage, 45 V sampling cone, 4 V extraction cone, and 150 and 500 (°C) source and desolvation temperature, respectively. Leucine enkephalin was used as the lock mass (*m/z* 556.2771) at a concentration of 500 pg/μL.

LogD$_{7.4}$ Measurement. After tracer elution from a C-18 light Sep Pak column, 500 mL of eluate (octanol) was mixed with an equal volume of 1 M phosphate buffer (pH 7.4) and vigorously vortexed for 1 min and centrifuged (10 min, 17250*g*). Three 100 μL aliquots were drawn from the corresponding *n*-octanol and aqueous phases. The radioactivity in each phase was counted (Compugamma 1282 CS, LKB-Wallac, Finland). The experiments were performed in triplicate for each tracer batch; the average logD$_{7.4}$ value is reported.

In Vitro Ligand Stability Test. The in vitro stability tests were performed by dissolving the formulated tracers in PBS, saline, rat plasma, and human plasma and incubating these solutions at 37 °C. After 1 and 2 h of incubation, the solutions were analyzed by radio-TLC (R_f [^{18}F]-**10a** = 0.4 and [^{18}F]-**10b** = 0.5, 14% acetonitrile in

dx.doi.org/10.1021/jm500700y | J. Med. Chem. 2014, 57, 6765−6780

chloroform). The rat and human plasma samples were deproteinized by adding 3 volumes of acetonitrile and centrifuged (5 min at 17250*g*) before they were used for analysis. After elution with the mobile phase, the TLCs were dried and placed on phosphor storage plates, which were later scanned with a Cyclone imaging system (PerkinElmer). The percentage of conversion as a function of incubation time was calculated by ROI analysis using Optiquant (version 3.00).

In Vivo and In Vitro Selectivity. Nonradioactive A_{2A}R-selective **12** [1 mg/kg, 50% dimethylacetamide (DMA): saline (v/v)] or vehicle (1 mL/kg, 50% DMA:saline)[32] were intraperitoneally administered 5−6 min prior to the intravenous injection of [^{18}F]tracers. In the in vitro ARG experiments, 2 μM (0.77 mg) **12** was used as a blocking agent.

In Vitro ARG Experiment. Isolated frozen brains of young (10−12 weeks of age; 300−350 g body weight) male Sprague−Dawley rats (Harlan, The Netherlands) were cut into two halves along the sagittal symmetry plane. Each half was mounted on paper slides with its lateral side up using Tissue-Tek fixing gel (Sakura, The Netherlands). After fixing, the brain was cut sagittally into 20 μm thick cryostat sections using a Leica CM 1950 cryostat (Leica Biosystems, The Netherlands) at −15 °C. The slices were thaw-mounted onto starfrost (76 × 26 mm, Waldemar Knittel, Germany) adhesive precoated slides, air-dried for 30−40 min and stored at −80 °C until they were used (within 1 week).

The slices were brought to room temperature and preincubated for 15 min in an assay buffer (50 mM Tris-HCl at pH 7.5 with 10 mM $MgCl_2$ and 1% bovine serum albumin). After preincubation, the slides were placed into jars with an assay buffer containing an approximately 5 nM radioligand [[^{18}F]-**10a**: 4.5 ± 1.5 nM (n = 3), 1.2 MBq and [^{18}F]-**10b**: 5.1 ± 1.8 nM (n = 5), 1.02 MBq]. To test the specificity of the binding, a 2 μM compound, **12**, was added to the buffer in one of the jars. The slices were incubated for 90 min at 37 °C. After incubation, the slices were washed for 5 min with ice-cold 0.01% Triton X in PBS. They were dipped in ice-cold water for 30 s to remove buffer salts and dried under a stream of air at room temperature. After drying, the slices were placed on phosphor storage screens for 8−10 h. The screens were then read using a Cyclone imaging system (Packard Instrument Co.). Optiquant (version 3.00) was used to quantify radioactivity. Regions of interest (ROIs) were drawn manually on the striatum and cerebellum. The regional uptake of radioactivity was measured and expressed as digital light units (DLU)/mm^2.

In Vivo Studies. *Animals and Study Design.* The animal experiments were carried out in compliance with the Law on Animal Experiments of The Netherlands. The institutional animal ethics committee approved the protocols. Male outbred Wistar-Unilever rats were obtained from Harlan (The Netherlands). The animals were housed in Macrolon cages (38 × 26 × 24 cm), maintained in a 12 h light−dark regime, and fed with standard laboratory chow (RMH-B, The Netherlands) and tap water ad libitum. After arrival, the rats were allowed to acclimatize for at least 7 days. For each tracer, the animals were divided into two groups, as follows. Group 1, vehicle-controls ([^{18}F]-**10b** (n = 6): body weight = 295 ± 19 g and injected dose = 0.21 ± 0.11 nM; [^{18}F]-**10a** (n = 5): body weight = 312 ± 14 g and injected dose = 1.13 ± 0.41 nM) and group 2, pretreated group ([^{18}F]-**10b** (n = 6): body weight = 293 ± 31 g and injected dose = 0.29 ± 0.27 nM; [^{18}F]-**10a** (n = 5): body weight = 321 ± 15 g and injected dose = 0.74 ± 0.62 nM).

Micro PET Scanning. Two animals were scanned simultaneously in each scan session (Supine position) using a Focus 220 MicroPET camera (CTI, Siemens, Munich, Germany). All animals were anesthetized with isoflurane/air (induction: 5% isoflurane, later reduced to ≤2%) and kept on electronic heating pads during the entire study period. Cannulas were placed in a femoral artery and vein for blood sampling and tracer injection (Harvard-style pump; 1 mL/min). The brain was in the field of view. A transmission scan of 515 s was made before the emission scan, using a rotating ^{57}Co point source. The emission data were acquired in list mode for 106 min, starting at the moment of tracer entering the body of the first rat; the second animal was injected 16 min later. PET data were corrected for attenuation, scatter, random coincidences, and radioactive decay and reconstructed in 25 time frames (8 × 30, 3 × 60, 2 × 120, 2 × 180, 3 × 300, 5 × 600, 1 × 480, and 1 × 960 s) using a 2D ordered subsets expectation maximization (OSEM) algorithm (4 iterations, zoom factor, 2). The reconstructed images were smoothed with a 3D Gaussian filter [1.35 mm full width at half-maximum (fwhm)].

During the scan, arterial blood samples (volume 0.1−0.15 mL) were drawn using a standard protocol (at 0, 5, 10, 15, 20, 30, 45, 60, 75, and 90 s and 2, 3, 5, 7, 10, 15, 30, 60, and 90 min after injection). After collecting 25 μL of whole blood, plasma (25 μL) was acquired from the remainder of the blood samples by a short centrifugation (5 min at 1000*g*). The radioactivity in 25 μL of plasma and whole blood was counted on a Compugamma γ-counter (1282 CS, LKB-Wallac, Turku, Finland), and the count statistics were then used as an arterial input function. The heart rates and blood oxygenation of the experimental animals were continuously monitored using pulse oximeters throughout the scanning procedure (Nonin Zevenaar, The Netherlands).

MicroPET Data Analysis. Time activity curves (TACs) for the frontal cortex, striatum, midbrain, cerebellum, and hippocampus were determined using Inveon Research Workplace (Siemens Medical Solutions, Knoxville, TN). The summed PET data from each animal were coregistered to an MRI template of the rat brain with predefined volumes of interest (VOIs). Translation, rotation, and scaling were adjusted to visually optimize the fusion of the images. The VOIs were transferred from the MRI template to the PET data, and regional TACs were generated. Standardized uptake values (SUVs) were plotted as a function of time, using body weights and injected doses.

Ex Vivo Biodistribution. After the PET-scan, the animals were sacrificed by the extirpation of the heart. Blood was collected from the animals, and plasma and a cell fraction were obtained from the sample by a short centrifugation (5 min at 1000*g*). Several tissues were excised and weighed. The radioactivities in the tissue samples and in a sample of tracer solution (infusate) were measured using a calibrated gamma counter. The data were expressed as the SUV.

In Vivo Metabolite Analysis. Plasma samples taken at intervals of 2, 5, 10, 15, 30, 60, and 90 min were used for metabolite analysis. Protein was removed by adding 3 volumes of acetonitrile followed by centrifugation (5 min at 17250*g*). Samples (2.5 μL) of the supernatant and infusate (internal standard, diluted 50 to 100 times) were loaded onto a TLC plate. After development with 15% acetonitrile in chloroform, the plate was dried and placed on a phosphor screen which was later read by the Cyclone system. ROIs were drawn manually on the parent and metabolite spots. The concentration of the parent tracer was expressed as the percentage of total radioactivity in the acetonitrile extract. Optiquant was used for radioactivity quantification.

Statistical Analysis. All results are expressed as the mean ± SEM. The differences between groups were examined using an unpaired two-tailed t test. $P < 0.05$ was considered to be statistically significant.

AUTHOR INFORMATION

Corresponding Author

*Address: Department of Nuclear Medicine and Molecular Imaging, University Medical Center Groningen, University of Groningen, Hanzeplein 1, 9713GZ, Groningen, The Netherlands. Tel: +3150 3613247. Fax: +31-50-3611687. E-mail: p.h.elsinga@umcg.nl.

Notes

The authors declare no competing financial interest.

ACKNOWLEDGMENTS

This project was supported by De Cock Stichting and ZonMW (Grant 91111007, UHPLC-MS-TOF). We thank Jurgen Sijbesma, MA Khayum and Marianne Schepers for their technical assistance.

ABBREVIATIONS USED

A_{2A}Rs, adenosine A_{2A} receptors; ARG, autoradiography; BBr_3, boron tribromide; BBB, blood-brain-barrier; BEH, ethylene-bridged hybrid; cAMP, cyclic adenosine monophosphate; $CDCl_3$, deuterated chloroform; CSPTC, cortico-striato-pallido-thalamocortical; D_2Rs, dopamine d2 receptors; ECL, extracellular loop; *g*, Earth's gravitational force; GOLD, a molecular docking software; Gs, heterotrimeric G protein; HLM, human liver microsome; K_{off}, dissociation rate constant $LogD_{7.4}$, octanol/buffer (pH 7.4) distribution coefficient; MicroPET, small-animal PET; nM, nanomolar; PTFE, polytetrafluoroethylene; QMA, quaternary ammonium anion; Q-Tof-Ms, quadrupole-time-of-flight-mass spectrometer; radio-TLC, radio-thin layer chromatography; ROIs, regions of interest; RP18, reverse phase 18; RP-HPLC, reverse-phase-high performance liquid chromatography; SUV, standardized uptake value; SEM, standard error of mean; TM's, transmembranes; TACs, time-activity curves; VOIs, volumes of interest

REFERENCES

(1) Estrela, A. B.; Abraham, W. R. Adenosine in the inflamed gut: A Janus faced compound. *Curr. Med. Chem.* **2011**, *18*, 2791−2815.

(2) Khanapur, S.; van Waarde, A.; Ishiwata, K.; Leenders, K. L.; Dierckx, R. A.; Elsinga, P. H. Adenosine A(2A) receptor antagonists as Positron Emission Tomography (PET) tracers. *Curr. Med. Chem.* **2014**, *21*, 312−328.

(3) Jacobson, K. A. Introduction to adenosine receptors as therapeutic targets. *Handb. Exp. Pharmacol.* **2009**, *193*, 1−24.

(4) Ralevic, V.; Burnstock, G. Receptors for purines and pyrimidines. *Pharmacol. Rev.* **1998**, *50*, 413−492.

(5) Ben, D.; Lambertucci, C.; Vittori, S.; Volpini, R.; Cristalli, G. GPCRs as therapeutic targets: A view on adenosine receptors structure and functions, and molecular modeling support. *J. Iran. Chem. Soc.* **2005**, *2*, 176−188.

(6) Fastbom, J.; Pazos, A.; Palacios, J. M. The distribution of adenosine A1 receptors and 5′-nucleotidase in the brain of some commonly used experimental animals. *Neuroscience* **1987**, *22*, 813−826.

(7) Martinez-Mir, M. I.; Probst, A.; Palacios, J. M. Adenosine A2 receptors: Selective localization in the human basal ganglia and alterations with disease. *Neuroscience* **1991**, *42*, 697−706.

(8) Ji, X. D.; Stiles, G. L.; van Galen, P. J.; Jacobson, K. A. Characterization of human striatal A2-adenosine receptors using radioligand binding and photoaffinity labeling. *J. Recept. Res.* **1992**, *12*, 149−169.

(9) Parkinson, F. E.; Fredholm, B. B. Autoradiographic evidence for G-protein coupled A2-receptors in rat neostriatum using [3H]-CGS 21680 as a ligand. *Naunyn-Schmiedebert's Arch. Pharmacol.* **1990**, *342*, 85−89.

(10) Lindstrom, K.; Ongini, E.; Fredholm, B. B. The selective adenosine A2A receptor antagonist SCH 58261 discriminates between two different binding sites for [3H]-CGS 21680 in the rat brain. *Naunyn-Schmiedebert's Arch. Pharmacol.* **1996**, *354*, 539−541.

(11) Ongini, E.; Fredholm, B. B. Pharmacology of adenosine A2A receptors. *Trends Pharmacol. Sci.* **1996**, *17*, 364−372.

(12) Fredholm, B. B.; Ijzerman, A. P.; Jacobson, K. A.; Linden, J.; Muller, C. E. International Union of Basic and Clinical Pharmacology. LXXXI. Nomenclature and classification of adenosine receptors: An update. *Pharmacol. Rev.* **2011**, *63*, 1−34.

(13) Cunha, R. A.; Johansson, B.; Constantino, M. D.; Sebastiao, A. M.; Fredholm, B. B. Evidence for high-affinity binding sites for the adenosine A2A receptor agonist [3H] CGS 21680 in the rat hippocampus and cerebral cortex that are different from striatal A2A receptors. *Naunyn-Schmiedebert's Arch. Pharmacol.* **1996**, *353*, 261−271.

(14) Paul, S.; Elsinga, P. H.; Ishiwata, K.; Dierckx, R. A.; van Waarde, A. Adenosine A(1) receptors in the central nervous system: Their functions in health and disease, and possible elucidation by PET imaging. *Curr. Med. Chem.* **2011**, *18*, 4820−4835.

(15) Macedo, L.; Pinhal-Enfield, G.; Alshits, V.; Elson, G.; Cronstein, B. N.; Leibovich, S. J. Wound healing is impaired in MyD88-deficient mice: a role for MyD88 in the regulation of wound healing by adenosine A2A receptors. *Am. J. Pathol.* **2007**, *171*, 1774−1788.

(16) Feoktistov, I.; Biaggioni, I.; Cronstein, B. N. Adenosine receptors in wound healing, fibrosis and angiogenesis. *Handb. Exp. Pharmacol.* **2009**, *193*, 383−397.

(17) Blackburn, M. R.; Vance, C. O.; Morschl, E.; Wilson, C. N. Adenosine receptors and inflammation. *Handb. Exp. Pharmacol.* **2009**, *193*, 215−269.

(18) de Lera Ruiz, M.; Lim, Y. H.; Zheng, J. Adenosine A2A receptor as a drug discovery target. *J. Med. Chem.* **2014**, *57*, 3623−3650.

(19) Armentero, M. T.; Pinna, A.; Ferré, S.; Lanciego, J. L.; Müller, C. E.; Franco, R. Past, present and future of A2A adenosine receptor antagonists in the therapy of Parkinson's disease. *Pharmacol. Ther.* **2011**, *132*, 280−299.

(20) Morelli, M.; Carta, A. R.; Jenner, P. Adenosine A2A receptors and Parkinson's disease. *Handb. Exp. Pharmacol.* **2009**, *193*, 589−615.

(21) Popoli, P.; Pepponi, R. Potential therapeutic relevance of adenosine A2B and A2A receptors in the central nervous system. *CNS Neurol. Disord.: Drug Targets* **2012**, *11*, 664−674.

(22) Ribeiro, J. A.; Sebastião, A. M.; de Mendonça, A. Adenosine receptors in the nervous system: Pathophysiological implications. *Prog. Neurobiol. (N. Y.)* **2002**, *68*, 377−392.

(23) Jacobson, K. A.; Gao, Z. G. Adenosine receptors as therapeutic targets. *Nat. Rev. Drug Discovery* **2006**, *5*, 247−264.

(24) Palacios, N.; Gao, X.; McCullough, M. L.; Schwarzschild, M. A.; Shah, R.; Gapstur, S.; Ascherio, A. Caffeine and risk of Parkinson's disease in a large cohort of men and women. *Mov. Disord.* **2012**, *27*, 1276−1282.

(25) Cao, C.; Loewenstein, D. A.; Lin, X.; Zhang, C.; Wang, L.; Duara, R.; Wu, Y.; Giannini, A.; Bai, G.; Cai, J.; Greig, M.; Schofield, E.; Ashok, R.; Small, B.; Potter, H.; Arendash, G. W. High blood caffeine levels in MCI linked to lack of progression to dementia. *J. Alzheimer's Dis.* **2012**, *30*, 559−572.

(26) Parent, A.; Hazrati, L. N. Functional anatomy of the basal ganglia. I. The cortico-basal ganglia-thalamo-cortical loop. *Brain Res. Rev.* **1995**, *20*, 91−127.

(27) Hamani, C.; Saint-Cyr, J. A.; Fraser, J.; Kaplitt, M.; Lozano, A. M. The subthalamic nucleus in the context of movement disorders. *Brain* **2004**, *127*, 4−20.

(28) Asanuma, K.; Tang, C.; Ma, Y.; Dhawan, V.; Mattis, P.; Edwards, C.; Kaplitt, M. G.; Feigin, A.; Eidelberg, D. Network modulation in the treatment of Parkinson's disease. *Brain* **2006**, *129*, 2667−2678.

(29) Bauer, A.; Ishiwata, K. Adenosine receptor ligands and PET imaging of the CNS. *Handb. Exp. Pharmacol.* **2009**, *193*, 617−642.

(30) Holschbach, M. H.; Olsson, R. A. Applications of adenosine receptor ligands in medical imaging by positron emission tomography. *Curr. Pharm. Des.* **2002**, *8*, 2345−2352.

(31) Narendran, R.; Hwang, D. R.; Slifstein, M.; Talbot, P. S.; Erritzoe, D.; Huang, Y.; Cooper, T. B.; Martinez, D.; Kegeles, L. S.; Abi-Dargham, A.; Laruelle, M. *In vivo* vulnerability to competition by endogenous dopamine: Comparison of the D2 receptor agonist radiotracer (−)-N-[11C]propyl-norapomorphine ([11C]NPA) with the D2 receptor antagonist radiotracer [11C]-raclopride. *Synapse* **2004**, *52*, 188−208.

(32) Hirani, E.; Gillies, J.; Karasawa, A.; Shimada, J.; Kase, H.; Opacka-Juffry, J.; Osman, S.; Luthra, S. K.; Hume, S. P.; Brooks, D. J. Evaluation of [4-O-methyl-(11)C]KW-6002 as a potential PET ligand for mapping central adenosine A(2A) receptors in rats. *Synapse* **2001**, *42*, 164−176.

(33) Ishiwata, K.; Noguchi, J.; Toyama, H.; Sakiyama, Y.; Koike, N.; Ishii, S.; Oda, K.; Endo, K.; Suzuki, F.; Senda, M. Synthesis and

preliminary evaluation of [11C]KF17837, a selective adenosine A2A antagonist. *Appl. Radiat. Isot.* **1996**, *47*, 507−511.
(34) Ishiwata, K.; Ogi, N.; Shimada, J.; Nonaka, H.; Tanaka, A.; Suzuki, F.; Senda, M. Further characterization of a CNS adenosine A2a receptor ligand [11C]KF18446 with in vitro autoradiography and in vivo tissue uptake. *Ann. Nucl. Med.* **2000**, *14*, 81−89.
(35) Marian, T.; Boros, I.; Lengyel, Z.; Balkay, L.; Horvath, G.; Emri, M.; Sarkadi, E.; Szentmiklosi, A. J.; Fekete, I.; Tron, L. Preparation and primary evaluation of [11C]CSC as a possible tracer for mapping adenosine A2A receptors by PET. *Appl. Radiat. Isot.* **1999**, *50*, 887−893.
(36) Noguchi, J.; Ishiwata, K.; Wakabayashi, S.; Nariai, T.; Shumiya, S.; Ishii, S.; Toyama, H.; Endo, K.; Suzuki, F.; Senda, M. Evaluation of carbon-11-labeled KF17837: A potential CNS adenosine A2a receptor ligand. *J. Nucl. Med.* **1998**, *39*, 498−503.
(37) Stone-Elander, S.; Thorell, J.; Eriksson, L.; Fredholm, B. B.; Ingvar, M. In vivo biodistribution of [N-11C-methyl]KF 17837 using 3-D-PET: Evaluation as a ligand for the study of adenosine A2A receptors. *Nucl. Med. Biol.* **1997**, *24*, 187−191.
(38) Wang, W. F.; Ishiwata, K.; Nonaka, H.; Ishii, S.; Kiyosawa, M.; Shimada, J.; Suzuki, F.; Senda, M. Carbon-11-labeled KF21213: A highly selective ligand for mapping CNS adenosine A(2A) receptors with positron emission tomography. *Nucl. Med. Biol.* **2000**, *27*, 541−546.
(39) Fujita, M.; Innis, R. B. In vivo molecular imaging: Ligand development and research applications. In *Neuropsychopharmacology: The Fifth Generation Of Progress*; Davis, K., Charney, D., Coyle, J., Nemeroff, C., Eds.; Lippincott, Williams, & Wilkins: Philadelphia, PA, 2002; pp 411−425.
(40) Leopoldo, M.; Lacivita, E.; De Giorgio, P.; Contino, M.; Berardi, F.; Perrone, R. Design, synthesis, and binding affinities of potential positron emission tomography (PET) ligands with optimal lipophilicity for brain imaging of the dopamine D3 receptor. Part II. *Bioorg. Med. Chem.* **2009**, *17*, 758−766.
(41) Pike, V. W. PET radiotracers: Crossing the blood-brain barrier and surviving metabolism. *Trends Pharmacol. Sci.* **2009**, *30*, 431−440.
(42) Amini, N.; Nakao, R.; Schou, M.; Halldin, C. Identification of PET radiometabolites by cytochrome P450, UHPLC/Q-ToF-MS and fast radio-LC: Applied to the PET radioligands [11C]flumazenil, [18F]FE-PE2I, and [11C]PBR28. *Anal. Bioanal. Chem.* **2013**, *405*, 1303−1310.
(43) Todde, S.; Moresco, R. M.; Simonelli, P.; Baraldi, P. G.; Cacciari, B.; Spalluto, G.; Varani, K.; Monopoli, A.; Matarrese, M.; Carpinelli, A.; Magni, F.; Kienle, M. G.; Fazio, F. Design, radiosynthesis, and biodistribution of a new potent and selective ligand for in vivo imaging of the adenosine A(2A) receptor system using positron emission tomography. *J. Med. Chem.* **2000**, *43*, 4359−4362.
(44) Moresco, R. M.; Todde, S.; Belloli, S.; Simonelli, P.; Panzacchi, A.; Rigamonti, M.; Galli-Kienle, M.; Fazio, F. In vivo imaging of adenosine A2A receptors in rat and primate brain using [11C]-SCH442416. *Eur. J. Nucl. Med. Mol. Imaging* **2005**, *32*, 405−413.
(45) Mihara, T.; Noda, A.; Arai, H.; Mihara, K.; Iwashita, A.; Murakami, Y.; Matsuya, T.; Miyoshi, S.; Nishimura, S.; Matsuoka, N. Brain adenosine A2A receptor occupancy by a novel A1/A2A receptor antagonist, ASP5854, in rhesus monkeys: Relationship to anticataleptic effect. *J. Nucl. Med.* **2008**, *49*, 1183−1188.
(46) Matsuya, T.; Takuma, K.; Sato, K.; Asai, M.; Murakami, Y.; Miyoshi, S.; Noda, A.; Nagai, T.; Mizoguchi, H.; Nishimura, S.; Yamada, K. Synergistic effects of adenosine A2A antagonist and L-DOPA on rotational behaviors in 6-hydroxydopamine-induced hemi-Parkinsonian mouse model. *J. Pharmacol. Sci.* **2007**, *103*, 329−332.
(47) Shinkre, B. A.; Kumar, T. S.; Gao, Z. G.; Deflorian, F.; Jacobson, K. A.; Trenkle, W. C. Synthesis and evaluation of 1,2,4-triazolo[1,5-c]pyrimidine derivatives as A2A receptor-selective antagonists. *Bioorg. Med. Chem. Lett.* **2010**, *20*, 5690−5694.
(48) Bhattacharjee, A. K.; Lang, L.; Jacobson, O.; Shinkre, B.; Ma, Y.; Niu, G.; Trenkle, W. C.; Jacobson, K. A.; Chen, X.; Kiesewetter, D. O. Striatal adenosine A(2A) receptor-mediated positron emission tomographic imaging in 6-hydroxydopamine-lesioned rats using [(18)F]-MRS5425. *Nucl. Med. Biol.* **2011**, *38*, 897−906.
(49) Elsinga, P. H.; van Waarde, A.; Jaeggi, K. A.; Schreiber, G.; Heldoorn, M.; Vaalburg, W. Synthesis and evaluation of (S)-4-(3-(2′-[11C]isopropylamino)-2-hydroxypropoxy) −2H-benzimidazol −2-one ((S)-[11C]CGP 12388) and (S)-4-(3-((1′-[18F]-fluoroisopropyl)-amino)-2-hydroxypropoxy) −2H- benzimidazol-2-one ((S)-[18F]-fluoro-CGP 12388) for visualization of beta-adrenoceptors with positron emission tomography. *J. Med. Chem.* **1997**, *40*, 3829−3835.
(50) DalBen, D.; Lambertucci, C.; Marucci, G.; Volpini, R.; Cristalli, G. Adenosine receptor modeling: What does the A2A crystal structure tell us? *Curr. Top. Med. Chem.* **2010**, *10*, 993−1018.
(51) Jaakola, V. P.; Griffith, M. T.; Hanson, M. A.; Cherezov, V.; Chien, E. Y.; Lane, J. R.; Ijzerman, A. P.; Stevens, R. C. The 2.6 angstrom crystal structure of a human A2A adenosine receptor bound to an antagonist. *Science* **2008**, *322*, 1211−1217.
(52) Alfaro, T. M.; Vigia, E.; Oliveira, C. R.; Cunha, R. A. Effect of free radicals on adenosine A(2A) and dopamine D2 receptors in the striatum of young adult and aged rats. *Neurochem. Int.* **2004**, *45*, 733−738.
(53) Graves, A. P.; Brenk, R.; Shoichet, B. K. Decoys for docking. *J. Med. Chem.* **2005**, *48*, 3714−3728.
(54) Kumar, T. S.; Mishra, S.; Deflorian, F.; Yoo, L. S.; Phan, K.; Kecskes, M.; Szabo, A.; Shinkre, B.; Gao, Z. G.; Trenkle, W.; Jacobson, K. A. Molecular probes for the A2A adenosine receptor based on a pyrazolo[4,3-e][1,2,4]triazolo[1,5-c]pyrimidin-5-amine scaffold. *Bioorg. Med. Chem. Lett.* **2011**, *21*, 2740−2745.
(55) Pajouhesh, H.; Lenz, G. R. Medicinal chemical properties of successful central nervous system drugs. *NeuroRx* **2005**, *2*, 541−553.
(56) Rydberg, P.; Gloriam, D. E.; Zaretzki, J.; Breneman, C.; Olsen, L. SMARTCyp: A 2D method for prediction of cytochrome P450-mediated drug metabolism. *ACS Med. Chem. Lett.* **2010**, *1*, 96−100.
(57) Fredholm, B. B.; Cunha, R. A.; Svenningsson, P. Pharmacology of adenosine A2A receptors and therapeutic applications. *Curr. Top. Med. Chem.* **2003**, *3*, 413−426.
(58) *Sybyl*, version 7.1; Tripos Associates Inc.: St. Louis, MO, 2005.
(59) Sherali, H. D.; Ulular, O. Conjugate gradient methods using quasi-Newton updates with inexact line searches. *Journal of Mathematical Analysis and Applications* **1990**, *150*, 359−377.
(60) Gasteiger, J.; Marsili, M. Iterative partial equalization of orbital electronegativity: A rapid access to atomic charges. *Tetrahedron* **1980**, *36*, 3219−3228.
(61) Verdonk, M. L.; Cole, J. C.; Hartshorn, M. J.; Murray, C. W.; Taylor, R. D. Improved protein-igand docking using GOLD. *Proteins* **2003**, *52*, 609−623.